1-1-2011

Growth and Optical Characterization of Zinc Oxide Nanowires for Anti-reflection Coatings for Solar Cells

Martha Coakley
Portland State University

Growth and Optical Characterization of Zinc Oxide Nanowires for Anti-Reflection Coatings for Solar Cells

by

Martha Coakley

A thesis submitted in partial fulfillment of the
requirements for the degree of

Masters of Science
in
Physics

Thesis Committee:
Rolf Könenkamp, Chair
Andres La Rosa
Andrew Rice

Portland State University
2011

Abstract

The optical properties of solar cells greatly affect their efficiencies. Decreasing the broadband and directional reflectance of solar cells increases the solar irradiance transmitted and absorbed by the cell, thereby increasing the production of electron-hole pairs. Traditional optical enhancements such as light trapping and anti-reflection coatings reduce the reflectance of silicon at an optimized wavelength and angle of incidence. They do not perform as well at high angles of incidence or over the broadband solar spectrum. Theoretical studies suggest that layers with a suitable gradient-index of refraction can create both a broadband and directional anti-reflective coating. Through their variations in height and tapered growth, Zinc oxide (ZnO) nanowires can create a gradient index anti-reflection coating. ZnO is a wide-band gap semiconductor that is non-absorbing over most of the solar spectrum. With low cost, low temperature techniques, ZnO nanowires can be grown with a variety of morphologies.

ZnO nanowires were grown by aqueous chemical growth and by electrodeposition on silicon to create a gradient-index anti-reflective coating for solar cell applications. The nanowire arrays were characterized using SEM images, goniometer scattering measurements, and integrating sphere total reflectance measurements. ZnO nanowires grown by aqueous chemical growth on silicon had average diameters between 60 nm and 100 nm and average lengths between 800 nm and 1100 nm. The nanowires had vertical alignment. They exhibited relatively small diffuse reflectivities and relatively large specular reflectivities. ZnO nanowires grown by electrodeposition had greater variances in length and diameter, with average diameters between 85 nm and 180 nm and average lengths between 500 nm and 1200 nm. Electrodeposited ZnO nanowires were randomly

arrayed and exhibited relatively large diffuse reflectivities and relatively small specular reflectivities. Total reflectance measurements showed that all nanowire arrays reduced the broadband reflectance of silicon. Smaller nanowire arrays outperformed the larger crystal growths. A five-fold decrease in the broadband reflectance of silicon was obtained from both vertical and randomly oriented nanowire arrays. The reflectances were constant for angles of incident below 35°. Measurements at angles of incidence greater than 35° are required to determine whether ZnO nanowires can perform as directional anti-reflective coatings and whether the morphology of the nanowires affects the directional reflectances.

ACKNOWLEDGEMENTS

- The Green Building Laboratory, Department of Engineering, Portland State University, for the use of the Lambda 950 UV/VIS/NIR spectrometer with integrating sphere. Thank you to Dr. David Sailor, Matt Grooves, and Seth Moody for their time and assistance.

- Pacific Northwest National Laboratory, Richland, Washington, for the use of the Fluorolog III spectrometer with integrating sphere. The research was performed at EMSL, a national scientific user facility sponsored by the Department of Energy's Office of Biological and Environmental Research. Thank you to Dr. Zheming Wang for his assistance.

- Athavan Nadarajah for taking all SEM images presented in this report.

Appreciation and thanks to the following individuals:

- Dr. Rolf Koenenkamp for his expertise, guidance, and advice in this research.
- Dr. Andres LaRosa and Dr. Andrew Rice for their time and participation as part of the thesis committee.
- Athavan Nadarajah for his assistance in experimental growths and for his thoughtful advice.
- Dr. Robert Word for his insights and suggestions.
- Dr. James A. Coakley, Jr. for extensive editing and advice.

TABLE OF CONTENTS

LIST OF TABLES

LIST OF FIGURES

1. Introduction

Solar cells are at the forefront of alternative energy development. With a growth rate of close to 30%, photovoltaic technology is considered one of the fastest growing fields, and in the face of fossil fuel shortages, the most viable future source of energy [1]. Solar cells generate energy when photons excite electron-hole pairs in a material. Electron-hole pairs are separated by a built in potential difference at a p-n junction in a device, and are transported via electrical contacts to an external circuit.

Silicon, the most developed photovoltaic material, is reaching its theoretical limits for solar energy conversion. There is a focus on creating more efficient solar cells by creating multi-junction cells, using quantum-wells, and developing thin film cells that are less expensive and use fewer materials. A large element of solar cell improvement is creating cells that better exploit the solar spectrum. As photovoltaic technology enters its next generation of engineering and research, one important area of solar cell development is improving the optical properties of the cell.

The optical properties of a solar cell determine how much light enters the cell and thus, the quantity of light capable of generating an electron-hole pair. The sun movement and broadband solar spectrum provide a range of incident angles and wavelengths. Thus, improving optical properties optimizes the structure of the cell to admit light at a larger range of angles and energies.

The two conventional ways to improve the optical properties of solar cells are by light trapping and anti-reflection coatings. These methods increase the amount of light which enters a cell, but are limited in their ability to exploit the broadband spectrum or

account for the movement of the sun. Using nanowires to create a gradient index anti-reflection coating will optimize the amount of solar radiation capable of entering a cell. A brief overview of light trapping techniques and anti-reflection coatings leads to the motivation for current research in the use of nanowires for anti-reflective coatings in solar cells.

1.1 Optical enhancement for solar cells

Silicon, the most developed photovoltaic material, has a relatively high reflectivity and poor absorption properties [2]. Light trapping structures and Anti-reflection (AR) coatings improve the efficiency of silicon solar cells by increasing the amount of light which enters and remains in the cell and thus able to generate an electron-hole pair.

Light trapping structures are geometric structures such as pyramids or random Lambertian surfaces made on the silicon surface by etching or mechanical grooving. The randomization of light as it enters the solar cell causes it to be "trapped" by total internal reflection. Transmission into the cell is also enhanced by multiple reflections of light within the light trapping structure, shown in Figure 1a.

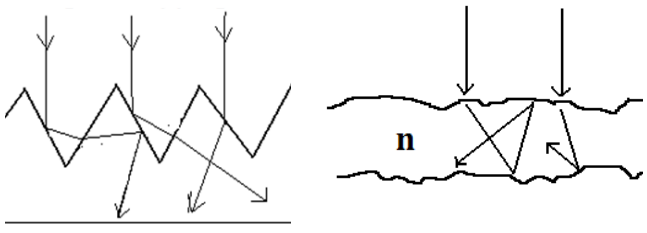

(a) **(b)**

Figure 1. (a) Light trapping from multiple reflections of incoming light and total internal reflection. (b) Pathlength enhancement with a Lambertian surface.

Lambertian surfaces, considered to be any non-periodic rough scattering surface, can theoretically enhance the path-length of light inside a material by $4n^2$, where n is the index of refraction of the material [3]. The path-length enhancement can be derived using geometric optics or statistical mechanics, and is modeled using computer ray-tracing programs [4]. For silicon, this leads to a path- length enhancement factor of 50. The absorption enhancement as a function of the wavelength, $a_I(\lambda)$, can calculated as:

$$a_I(\lambda) = \frac{a(\lambda)}{a(\lambda) + \frac{1}{4n^2 W}}$$

The absorption increases as a function of the width of the cell, W [3]. The dependence of the absorption on the path-length enhancement factor and the width has enabled solar cells to use a thinner silicon substrate with light trapping structures and maintain solar cell efficiency. Experimentally, light trapping structures have improved the efficiency of solar cells by up to 4% [4, 5].

The second optical enhancement technique for solar cells is anti-reflection (AR) coatings, which are based on the principle of interference between incident and reflected light. Matching boundary conditions for electromagnetic radiation at the interface of two dissimilar media will lead to Fresnel equations [6-8], which can be solved for the reflected and transmitted light at an interface. For TE (s-polarized) and TM (p-polarized) polarized light the reflectance of silicon varies as a function of angle (Figure 2).

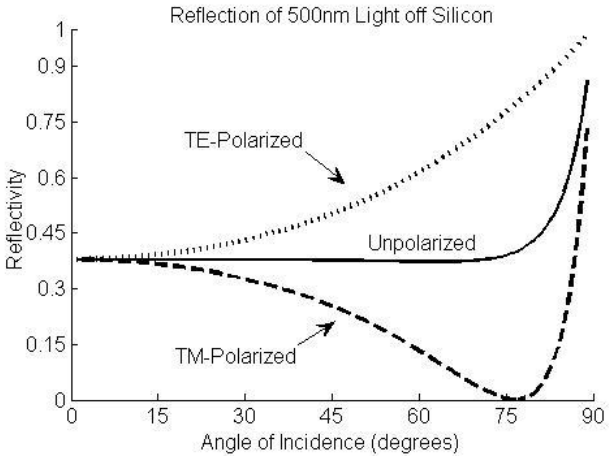

Figure 2. Reflectivity of silicon as a function of angle according to Fresnel equations.

When a thin AR layer is placed on the silicon surface, the Fresnel equations can be applied to both surfaces to solve for the total reflectance. The width of the thin layer will correspond to a phase change between the reflected waves from each surface. If the two reflections are out of phase then destructive interference will occur at the first interface and all incident energy is transmitted.

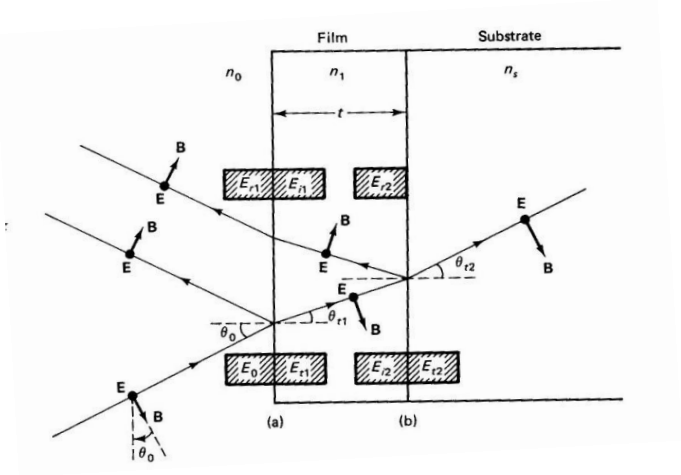

Figure 3. Matching of boundary conditions leads the energy of reflected and transmitted waves [8].

Single layer AR coatings are made a quarter-wavelength optical thickness to create a half-wavelength path difference between the reflections of normal incident light, creating the destructive interference. For a quarter-wavelength coating and normal incident light, the reflectance from a single layer coating can be simplified to be: $R = \frac{(n_0 n_s - n_1^2)^2}{(n_0 n_s + n_1^2)^2}$, where n_o, n_1, and n_s represent the refractive indices for the incident media, thin layer coating and substrate, respectively. There will be zero reflection when: $n_0 n_s = n_1^2$ or $n_1 = \sqrt{n_0 n_s}$. For 500 nm light, the optimized index of refraction for an AR coating for silicon would be $n_1 = 2.07$. Table 1 lists indices of refraction for materials commonly used as AR coatings.

Table 1. AR Coating Materials for Silicon: Single and Multilayer Coatings

Typical AR coating material	ZnS	TiO_2	Ta_2O_5	SiO_2	MgF_2	ITO
Index of refraction	2.5	2.3-2.7	2.2	1.5	1.38	2.0

Common single layer AR coatings for silicon solar cells are titanium dioxide and indium-tin oxide, which have indices of refraction between 2 and 3. For multi-layer AR coatings, the reflection from thin film coatings can be calculated using the transfer matrix methods for electromagnetic waves [8]. Multilayer coatings perform better than single layers because of the interference between layers, as shown in Figure 4.

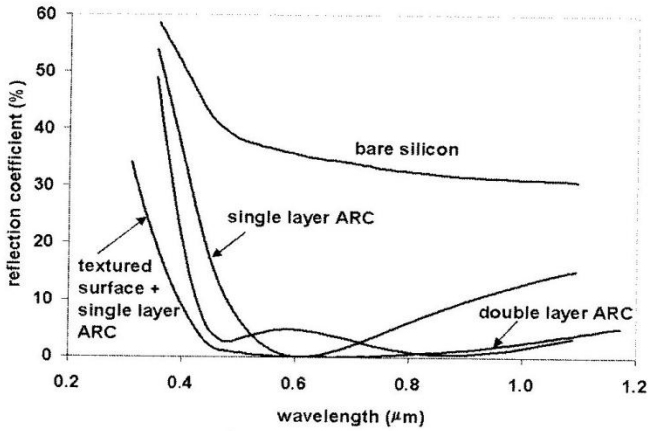

Figure 4. Effectiveness of different AR coatings (ARCs) on silicon. [9]

A combination of these two optical enhancement techniques, light trapping and AR coatings, is used for solar cells. A typical silicon solar cell may have pyramidal front and back surfaces with a quarter-wavelength AR coating. However, both optical enhancement methods have drawbacks. Light trapping structures are made by mechanical grooving or chemical etching of the solar cell surface. Mechanical grooving can be expensive and time intensive, and etching with substances such as hydrofluoric acid (50%): nitric acid (65%): acetic acid (96%) leads to toxic chemical by-products [5]. Single layer AR coatings fail to exploit all wavelengths and all angles of the incident sunlight. On the other hand, improving AR coatings by adding multiple layers increases manufacturing costs.

Improving the optical properties of solar cells will increase their efficiency, but at the same time, the fundamental structure of solar cells is changing. Current solar cells such as thin films, p-i-n junction cells, organic solar cells, and multi-junction devices are made from an array of materials such as InP, GaAs, and CdTe. Nanostructured materials represent a promising area for solar cell development. The use of nanostructures in solar

devices could mean using fewer materials, creating more versatile structures such as flexible solar devices, and exceeding the efficiency of traditional "bulk" cells. Improving the optical properties of solar cells should parallel the evolution of their structure. Nanostructures could be used to create gradient index AR coatings that could be applied to a variety of solar cell structures.

1.2 Gradient index optical coatings

A novel way to create an omni-directional and broadband AR coating is to make a gradient index of refraction coating using multiple thin layers or nanoporous media. Gradient index of refraction materials have been used since the 1850s, to correct aberration in lenses and create light propagation in fiber optic cables [10]. Gradient index optics takes advantage of the gradual curvature of light as it passes through a material. The effect was observed by Lord Rayleigh, who solved for a gradient between two media after observing that the reflection due to a gradual change in media must be less than that of an abrupt change [11]. The atmosphere is often cited as a gradient index media, where light bends due to the change in air density.

A gradient index of refraction can be modeled using the transfer matrix method for multi-layer films [6-8, Appendix 3]. Splitting the gradient layer into slabs parallel to the surface, an effective index of refraction can be found for each layer using Effective Media Approximation (EMA) [12]. Using the index of refraction for each of these layers, the reflection for each thin layer surface can be calculated. It is necessary to solve Maxwell's equations since the dimensions of the structures are much less than the wavelength of light, and render geometric approximations inappropriate.

In the 1980s it was found that a quintic gradient index profile could reduce reflection from a surface better than a linear gradient coating [13]. The quintic profile is given by:

$$n_Q(z) = n_{max} - (n_{max} - n_{min})\left[10\left(\frac{z}{d}\right)^3 - 15\left(\frac{z}{d}\right)^4 + 6\left(\frac{z}{d}\right)^5\right]$$

where n_{max} is the maximum index of refraction, n_{min} is the minimum (incident) index of refraction, *d* is the thickness of the layer, and *z* the depth into the layer. The profile represents a continuously varying media. The composite coating is referred to as an inhomogeneous layer (Figure 5).

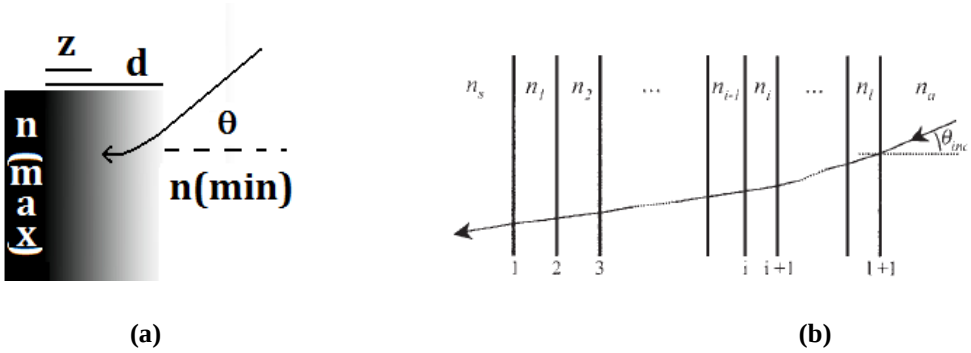

(a) **(b)**

Figure 5. (a) Gradient index profile, labeled according to a quintic profile. (b) Splitting of a gradient index profile into thin layers to apply the transfer matrix method for thin films [14].

Modifications of the quintic profile have been made to take into account grazing angles of incidence [14], which may also be improved by exponential and Gaussian index profiles [15]. These profiles perform better at large angles of incidence by minimizing the change in angle as light propagates through each layer. However, they require thicker layers and may not perform as well for normal incident light. Figure 6. shows a quintic profile for silicon, which corresponds to a broadband reflectance under 1%. The profile was optimized for an index of refraction $n = 4.2$. However, as the wavelength changes,

the index of profile will also change, altering the quintic shape. This effect, however, will be small.

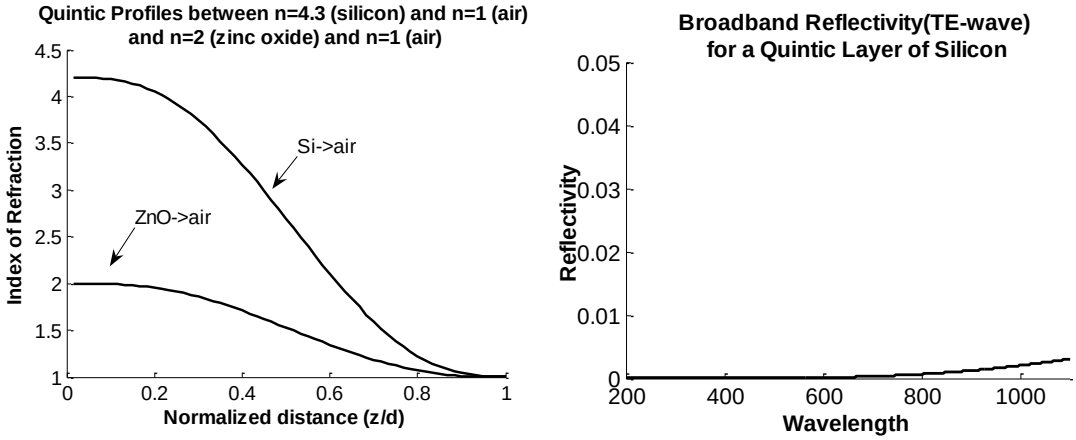

(a) **(b)**

Figure 6. (a) Quintic profiles for silicon (Si) to air and zinc oxide (ZnO) to air interfaces (b) Reflectivity for a TE wave calculated for a 1.2μm Si to air quintic interface using a transfer matrix method written for MATLAB, with a minimum of 15 layers per λ/4 optical thickness. It does not account for the shift in the profile due to the wavelength dependent index of refraction.

The manufacturing of gradient index anti-reflection layers remains difficult. One approach to such thin film layers is to coat them intermittently, using porous media to achieve a range of indices of refraction. Thin layer gradient index layers have been achieved using laser assisted evaporation and sputtering, but they require deposition techniques which can be expensive and time intensive to achieve ideal layers [16, 17]. Nanowires represent a way to create gradient index layers efficiently and inexpensively.

1.3 ZnO Nanowires as anti-reflection coatings for solar cells

Nanowires have been presented as a novel way to create a gradient index of refraction between two media. They can be grown with different orientations using a variety of techniques. Vertically orientated nanowires can create a graded index of

refraction either by tapering into a conical shape or by random height variations. Nanowires used as gradient-index AR coatings are different than the previously discussed quarter-wavelength optical coating and geometric light trapping techniques. Gradient-index nanowire layers are inhomogeneous and structures are smaller than the wavelength of incident light. To be effective, according to theoretical models, the nanowires should have a diameter much less than the wavelength of light, and have a minimum vertical length equivalent to at least $\lambda/2$ in optical thickness [16]. A variety of nanowires, nanorods, and other sub-wavelength structures have been grown using materials such as GaN, GaP, Si and ZnO. Nanowires are grown using a variety of methods such as epitaxial beam deposition, chemical vapor deposition, electron beam lithography, and etching [18-21]. The use of nanowires as part of the electronic structure of solar cells is widespread, and they have been shown to improve the optical and absorptive properties of the cells [22, 23]. Nonetheless, due to the large extent of this topic, research will be limited to the use of dielectrics as non-absorptive AR coatings.

Zinc oxide nanowires have been grown for anti-reflection coating for solar cells [24, 25]. The advantage of ZnO nanowires is that they can be grown using a variety of low temperature deposition techniques from inexpensive, non-toxic materials. The large band-gap of ZnO makes them a transparent, non-absorbing layer. Chen and Sun [24] have shown that ZnO nanorods grown using an aqueous chemical growth technique are capable of 10 percentage point reduction in the broadband reflection by a silicon device and a 2.4% improvement in its efficiency. Lee, et al. [25], explored the optical properties

of the nanowires resulting from tapering during the growth process and have achieved broadband reflectance by nanowires on silicon below 10%.

Vertical nanowire arrays can be simply modeled using Bruggemann's Effective Media Approximation (EMA) [19,22]. A vertical layer with random height variations or tapering can be split into thin horizontal slabs. Each slab has an effective index of refraction, n_{eff}, according to a volume fill factor. For a ZnO layer in ambient air, the EMA is: $f_{ZnO}\frac{n_{ZnO}^2 - n_{eff}^2}{n_{ZnO}^2 + 2n_{eff}^2} + (1 - f_{ZnO})\frac{n_{air}^2 - n_{eff}^2}{n_{air}^2 + 2n_{eff}^2} = 0$, where f_{ZnO} represents the percent volume filled with ZnO. Bruggemann's EMA is only valid for sub-wavelength structures and is contingent on the geometry of such structures [27].

1.4 Objectives of Research: Growth and characterization of ZnO nanowire arrays

ZnO nanowire arrays show promise as anti-reflection coatings for solar cells and can be deposited over large surface areas. The nanowires can be grown with a variety of methods with varying morphologies, diameters, lengths and densities. Unfortunately, there has been little experimental research into the effect of these morphologies on anti-reflection properties. Previous research has focused solely on the broadband properties of vertical ZnO arrays. It is unclear whether vertical ZnO nanowire arrays will perform better at different angles of incidence than a random ZnO nanowire orientation. The objective of this research is to investigate the effect of morphology on the anti-reflective properties of ZnO nanowire arrays.

Using two different chemical solution growth techniques, electrodeposition and aqueous chemical growth, ZnO nanowire arrays were grown on silicon. These growth methods are low cost, low temperature chemical solution techniques. The goal was to create such arrays without caustic chemicals and to use methods that can be scaled up to large surface areas. Nanowires were deposited on silicon so that relative reflectance comparisons could be made to a polished silicon substrate surface. Morphologies were characterized using scanning electron microscopy (SEM). Scattering and total reflectance measurements were taken using a goniometer and an integrating sphere.

Theory suggests that as nanowire arrays approach a quintic gradient index profile with respect to incident light, their performance as an AR coating improves. Although tapering the nanowires with chemicals is difficult, selective growth of nanowires that fit the desired profile may be possible. For this reason, growth methods were orientated toward creating longer, thinner wires, with larger height variations [15]. Comparisons of the different characteristic parameters of the wires with respect to the reduction in reflection by a silicon substrate may lead to an improved understanding of the way that light is scattered by the nanowires, and whether theoretical models can accurately reflect nanowire morphology.

2. Experimental Methods

2.1 Growth of ZnO Nanowires

ZnO is a II-VI semiconductor, with a direct band-gap of 3.37 eV. ZnO nanostructures are widely used in LEDs for their UV luminescence and in gas sensors and solar cells for their electron transport properties. Zinc oxide can be grown either as a hexagonal wurtzite crystal, cubic zincblende or cubic rock salt, as illustrated in Figure 7. A zincblende crystal, however, is only a stable when grown on other cubic lattices and rock salt is rare and must be grown under high pressure [28].

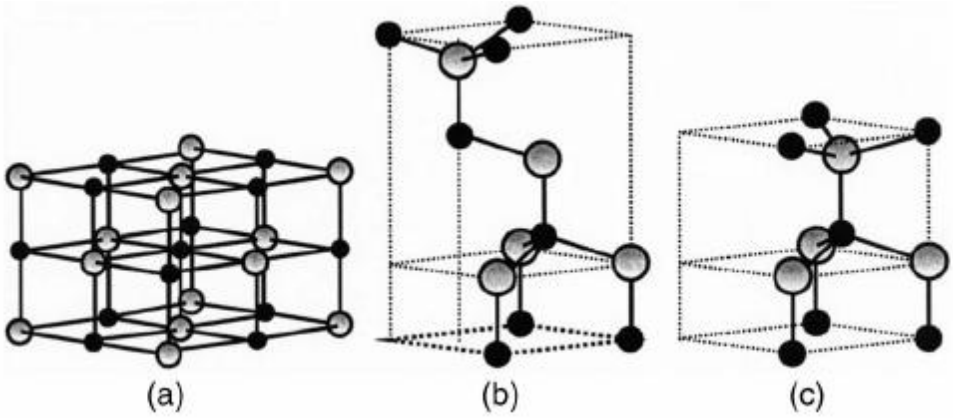

Figure 7. (a) Rock salt (b) Zincblende and (c) Hexagonal wurtzite structure for ZnO. [29]

Under ambient conditions, ZnO has a wurtzite crystal structure also called zincite. The zinc is tetrahedrally bonded to four oxygen atoms. Although a tetrahedral bond usually would be considered covalent sp^3, the bond is considered highly ionic due to the different electronegativities of the zinc and oxygen atoms. The lattice parameters of the crystal are a=3.2495 Å and c=5.2069 Å, where a extends in the basal plane, and c extends in the vertical plane. Alternating layers of Zn-O make up the crystalline structure. The c/a ratio varies from 1.593 to 1.6035, which is close to that of an ideal hexagonal

structure (c/a=1.63) [28-30]. Owing to the polar-face of the [001] plane, which is perpendicular to the c-axis as seen in Figure 8a, ZnO nanowires grow preferentially along the c-axis [31].

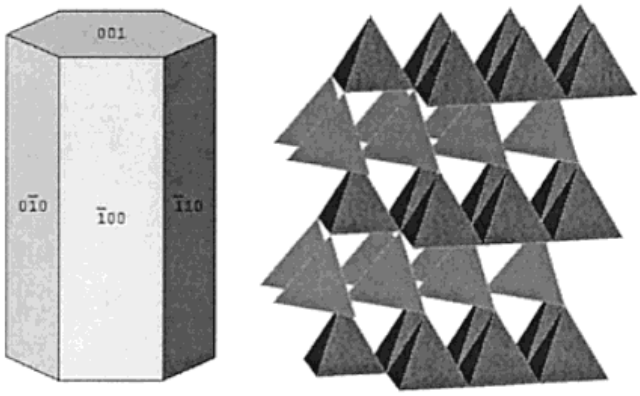

(a) **(b)**

Figure 8. (a) Hexagonal faces of wurtzite ZnO with c-axis [001] orientated growth and (b) Zincite crystal structure [31].

ZnO structures can be grown by a variety of deposition techniques, with diameters ranging from 50 nm to 200 nm and lengths exceeding 10 μm. Epitaxial deposition by vapor deposition techniques such as metal-organic chemical vapor deposition (MOCVD), pulse laser deposition (PLD) and vapor-liquid-solid (VLS) growth are often employed in research and industry [31, 32]. Although they allow for easy doping and control of growth parameters, these methods typically require vacuum systems and temperatures exceeding 800 ^{o}C. Two chemical solution techniques for growing ZnO nanostructures at low temperature have been developed: aqueous chemical growth and electrochemical deposition or simply referred to as electrodeposition. The advantage of using two different growth techniques is obtaining nanowires with different morphologies. Electrodeposited ZnO nanowires tend to have random orientation, whereas ZnO nanowires grown by aqueous chemical growth exhibit vertical orientation

2.1.1 Aqueous Chemical Growth

Aqueous chemical growth (ACG) of ZnO nanowires was developed by Vayssierres and Kleis [31] and is a thermal decomposition method. The method consists of equal molar mixtures of two chemicals, zinc nitrate hexahydrate ($Zn(NO_3)_2 \cdot 6\ H2O$) and hexamethylenetetramine, also called hexamine or methenamine ($C_6H_{12}N_4$), in de-ionized water. Both substances are stable, low cost, and pose minimal health risks. The aqueous bath is heated to 90 ^oC for a time span on the order of hours. SEM images and x-ray diffraction show ZnO wurtzite crystal presence with c-axis oriented growth [31]. The chemical reaction taking place is documented as:

(1) $C_6H_{12}N_4 + 6\ H_20 \rightarrow 4\ NH_3 + 6\ HCHO$

(2) $NH_3 + H_2O \leftrightarrow NH_4^+ + OH^-$

(3) $Zn^{2+} + 2\ OH^- \leftrightarrow Zn(OH)_2$

(4) $Zn(OH)_2 \rightarrow ZnO + H_2O$

In general, nitrate salts provide Zn^{2+} ions, and water provides O^{2-} ions. The exact role of the methenamine is not understood, only that the methenamine hydrolyzes slowly which controls the precipitation rate of the Zn^{2+} ions [33].

The concentrations of the bath, temperature of growth, pH of the solution, and time of deposition all affect the ZnO nanostructure morphology. For nanowire or nanorod growth, typical concentrations range from 0.001 M to 0.1 M, leading to control of wire diameter from 40 nm to 300 nm [32]. Height and diameter variations are also affected by temperature and pH. Decreasing temperature from 95 °C to 90 °C decreases the evaporation of ammonia from the solution, leading to larger nanowire diameters.

Experiments have also been performed directly manipulating the pH, where wires become flower like structures at a pH of 12 [35]. A pH of 6 to 7 is the optimum growth environment for ZnO nanowires. Growth time is proportional to both the diameter and vertical length of the nanowires. Samples can be placed in a new chemical bath to sustain growth rates [36, 37].

The ACG method is dependent on the polarity of the ZnO crystalline structure which allows for self-alignment in the hexagonal shape. Seeding the substrate prior to ACG with a planar ZnO layer has been found to produce dense, vertical nanowire growth. Depositing zinc acetate dihydrate dissolved in ethanol by spin coating [38] or spray pyrolysis [39] at low temperature creates a planar layer of ZnO.

Experimentally, the following methods were used to grow ZnO nanowires. An n-type (Sb doped) silicon substrate approximately 25 mm x 15 mm in dimension was used. Prior to growth the silicon was cleaned by sonication for 10 minutes in methanol, 10 minutes in acetone, and then rinsed with de-ionized water.

Before the growth of nanowires by ACG, a seed layer was deposited using the spray pyrolysis of 0.1 M zinc acetate dihydrate (99.99% purity, Sigma Aldrich) dissolved in ethanol, with 2% acetic acid and 4% deionized water by volume. The substrate was placed on a hot plate heated to 280 ^{o}C. Using an airbrush, layers were sprayed on the substrate every thirty seconds. The numbers of layers ranged from 10 to 40, with 40 layers yielding a uniform ZnO film. After spraying, the substrate was annealed at 380 ^{o}C for 20 minutes to guarantee the complete evaporation of ethanol.

Chemical bath growth was performed using 0.02 M zinc nitrate hexahydrate (99% purity, Sigma Aldrich) and 0.02 M methenamine (99.5% purity, Sigma Aldrich). The compounds were dissolved in de-ionized water and sonicated for 15 minutes to break up large crystals. A few samples were made using slightly lower and higher concentrations to study the effects on morphology. A set-up of the ACG growth is shown in Figure 9.

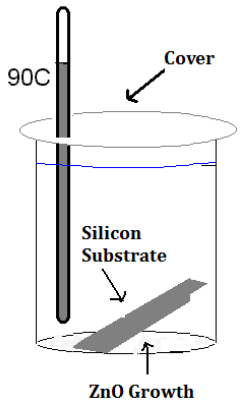

Figure 9. Growth of ZnO nanowires by Aqueous Chemical Growth (ACG) in a 0.02 M bath.

The substrate with the pre-growth layer was placed face down in 40 ml of the ACG solution and heated to 85 ^{o}C - 95 ^{o}C. Owing to the variability of the hot plate and the small volume of solution, maintaining a constant temperature at all times was difficult, The temperature could, however, be kept within the 85 ^{o}C - 95 ^{o}C range. The substrate sits at a tilted angle, with the seed layer facing the bottom. ZnO nanowire growth occurs on the bottom-facing surface. Mixing the solution was found to cause the deposition of large crystals on the sample. Placing samples face down in a stationary solution helped keep large crystals from falling onto the nanowires.

The bath was covered with aluminum foil to avoid excess evaporation. Evaporation would lead to a low pH, too low to support the desired nanowire growth. To counter the evaporation over time and replenish reactants, small amounts of the 0.02 M

solution were periodically added to maintain a constant volume. Growth time ranged from 3 hours to 5 hours, but was typically 4 hours for most samples. Following deposition the substrate was rinsed with de-ionized water and dried with nitrogen gas.

For two samples grown by ACG, a titanium dioxide (TiO_2) layer was spin-coated prior to the deposition of a seeding layer. TiO_2 has a higher index of refraction than ZnO and may create a step-layer between the ZnO and Si, leading to an improved AR coating. First, titanium (IV) isopropoxide was diluted to 10% by volume in isopropanol. The titanium solution was uniformly coated on a Si substrate by applying a spin-coating for 30 seconds at a spin-rate of 2500 RPM. The substrate was heated to 100 ^{o}C for 5 minutes to allow for slow evaporation of the isopropanol, and then annealed at 380 ^{o}C for 1 hour. Appendix 1 presents a complete table describing the particular growth conditions of each ACG ZnO nanowire sample. The results section discusses the resulting nanowires morphology and optical characteristics.

2.1.2 Electrodeposition

Electrodeposition of ZnO nanowires was performed following the method of Peulon and Lincot [41]. Electrodeposition is a method where a potential difference is created between a reference electrode, a positive anode, and negative cathode. The potential difference helps dissociate ions for a chemical reaction. By creating a potential difference in an aqueous chemical solution of $ZnCl_2$, bubbled with oxygen, ZnO crystals can form on a conductive substrate attached to the cathode. The following chemical reactions are known to take place:

(1) $O_2 + 2H_2O + 4e^- \rightarrow 4\ OH^-$

(2) $ZnCl_2 \rightarrow Zn^{2+} + 2\ Cl^-$

(3) $Zn^{2+} + \frac{1}{2} O_2 + 2e^- \rightarrow ZnO$ - 0.93 V/NHE

Reaction (3) takes place at the negatively charged cathode, where positive zinc ions combine with oxygen and hydroxide complexes and form nanowires. Potassium chloride (KCl) is added to the solution to improve the conductivity. Morphology of the nanowires is highly dependent on the solution pH, temperature, and the potential difference. Figure 10 depicts the set-up for the elecrodeposition of ZnO nanowires.

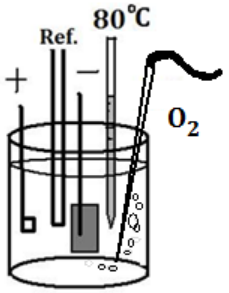

Figure 10. Schematic of electrodeposition of ZnO nanowires. A conductive substrate is attached to a negative cathode, where Zn^{2+} react with O_2.

In order for electrodeposition to work, the substrate must have a conductive layer to connect to the cathode. Unfortunately, the rapid formation of an oxide layer on the silicon surface impairs the electrodeposition of ZnO nanowires directly on silicon. As a result, the experimental growth of ZnO nanowires by electrodeposition was performed on silicon coated with ITO (Sn-doped indium oxide). ITO is a transparent conductive oxide layer with a large band-gap and is often used as an AR coating.

Growth conditions for ZnO nanowires were first found on ITO covered quartz glass, with the coating layer approximately 20 nm and a sheet resistance of 100 Ω/square. After determining conditions favorable to nanowire growth, ZnO nanowires were grown on ITO covered n-type (Sb doped) silicon substrates. The ITO had a sheet resistance of 100 Ω/square, with a transmittance ranging from 85% at 400 nm to 95% at 900 nm. Prior to deposition, the ITO/Si substrate was sonicated for 10 minutes each in methanol and acetone. The substrate was then rinsed with de-ionized water. For a few samples a pre-growth layer of planar ZnO layers was deposited using the spray pyrolysis of zinc acetate dihydrate, as outlined in ACG section. As a seeding layer was not necessary for growth of ZnO nanowires, electrodeposition was also carried out without this layer present.

Electrodeposition was performed using an EG&G Instrument from Princeton Applied Research Potentiostat/Galvanostat Model 283. The reference electrode was a Ag/AgCl electrode (0.2 V/NHE), while the cathode and anode were platinum wires. The platinum wires were cleaned with 0.1M HNO_3 prior to use. The ITO/Si substrate was attached to the cathode. Using the potentiostat method, the cathode was kept at -1.05 V relative to the reference electrode. The deposition solution was 0.3 mM $ZnCl_2$ (99.9% purity, Sigma Aldrich) and 0.1 M KCl (99.9% purity, Sigma Aldrich) in deionized water. The solution was bubbled with O_2 at a constant rate while being magnetically stirred. The solution was heated to 80 ^oC for a growth time of 1 hour. Following deposition the sample was rinsed with deionized water and dried with nitrogen gas. The results section discusses the properties of the nanowires grown by electrodeposition. Appendix 1 presents a table listing samples grown by electrodeposition and growth parameters.

2.2 Optical Characterization of ZnO Nanowires

2.2.1 SEM Images

A Scanning Electron Microscope (SEM) was used to characterize the morphology of ZnO nanowire arrays and seeding layers. The SEM images were useful in developing growth techniques, and in associating the scattering and reflectances of the wires with wire morphology. Images were made using a FEI Sirion XL30 SEM, which is capable of resolutions down to 1.5 nm. Images were usually made with a 20 kV electron beam at 30^{o} to 45^{o} incidence.

2.1.2 Goniometer

A goniometer with a photodiode was used to measure the angular dependent scattering by ZnO nanowire array samples. A goniometer can measure both the specular and diffuse reflectivity of samples. In the goniometer set-up, a laser was used to illuminate the sample and the light reflected by the sample was measured with a photodiode that rotated around the perimeter in the horizontal plane. The top-view graphic of the goniometer is shown in Figure 11. The entire system was kept under a black box to eliminate stray room-light. A 532nm, 1.8 mW diode laser with a collimated beam was used. The laser was chopped by a small fan at a frequency ranging from 105 Hz to 115 Hz. A silicon photodiode rotated on a 180 mm radial arm at incremental angle steps. The photodiode was 4 mm by 4 mm. A 1^{o} step size was sufficient to sample all reflection within the horizontal plane.

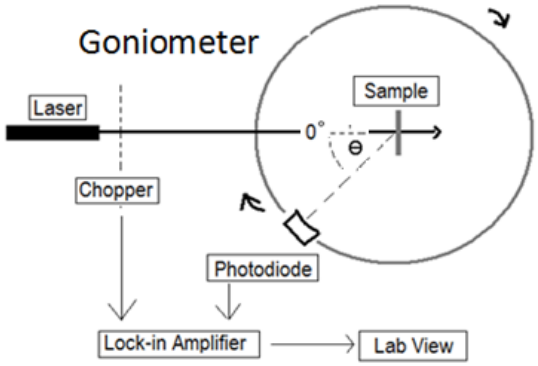

Figure 11. Top-view of the goniometer used to measure reflection by ZnO nanowires

The photodiode was oriented with its face perpendicular to the sample, to avoid light scattering from other surfaces or coming directly from the laser. A reflective piece of silicon or a glass beam splitter situated behind the photodiode was used to reflect light from the sample into the photodiode. The goniometer sample holder and photodiode arm were attached to separate stepper motors.

The current from the diode and the frequency from the chopper were fed into a Stanford Research Systems SR830 lock-in amplifier. The amplifier reduced noise from ambient light sources and was capable of measuring currents from 10^{-12} A to 10^{-6} A. At times, a neutral density filter was placed in front of the laser to attenuate signal. Attenuating the signal, I_o, with a 50 Ω resistor in parallel with the lock-in amplifier, however, often proved more effective. With the1000 Ω input impedance of the lock-in amplifier, the attenuated current I_a was equal to 0.0476 I_o. This attenuation was verified experimentally. A LabVIEW program received the current read from the lock-in amplifier and controlled the stepper-motors on the goniometer.

Two programs were used to take data. The first was a scatter scan. The sample was held normal to the incident laser beam while the photodiode moved incrementally to

collect the reflected light in the horizontal plane. A scatter scan provided measures of both diffuse and specular reflection of the sample. The measurements could be integrated assuming isotropic reflection to obtain the total reflectance. The difficulty of accurately measuring the amplitude of the specular peak for highly reflecting samples led to the conclusion that an integrating sphere was more reliable for total reflectance measurements.

The second type of scan was a specular peak scan. The sample was moved in incremental angles with respect to the laser with the photodiode measuring the specular reflection peak. A polarizer was placed in front of the laser to determine the specular reflectance for ZnO nanowire samples for both TE and TM polarized light.

2.2.3 Integrating Sphere

An integrating sphere has a diffusely reflection coating on its inner surface. The inner surface multiply reflects light that is incident on the sample, producing a diffuse radiance that is measured by a photodetector. Integrating spheres are used to measure the total reflectance, transmittance, and absorptance of a sample. In a substitution reflection measurement, where the sample is inserted into the sphere in place of a reflectance standard, the reflectance of the sample is calculated based on the change of radiance that hits the detector. Since the reflectance is calculated from diffuse radiance, the detector must not receive direct illumination from the sample. The detector is commonly protected by baffles or in a separate sphere compartment [41]. Figure 12 shows the configuration of a substitution integrating sphere.

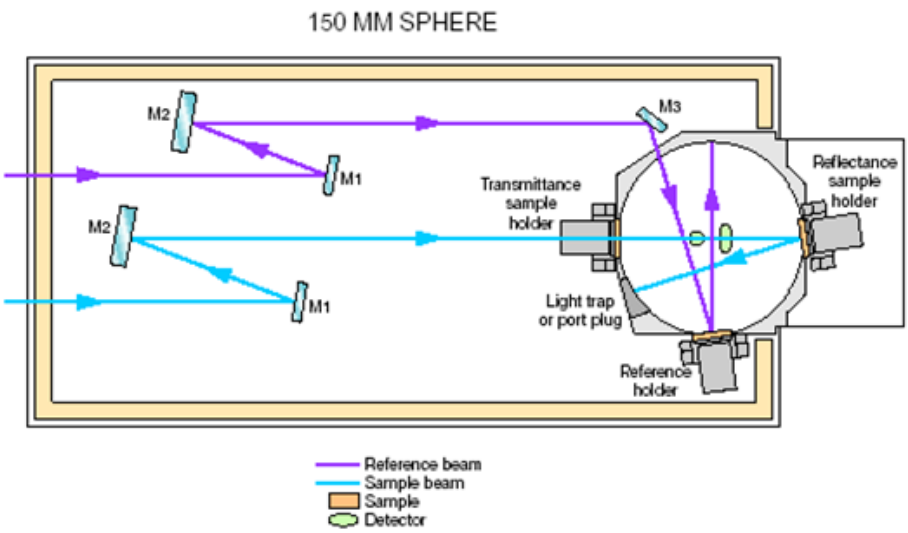

Figure 12. Design of Lambda 950 UV/VIS/NIR 150 mm integrating sphere [42].

Two integrating spheres were used to measure the reflectances of ZnO nanowire arrays. The first integrating sphere was a 150 mm integrating sphere attached to PerkinElmer 950 UV/VIS/NIR spectrometer. The spectrometer could be scanned from 300 nm to 1100 nm. It provided broadband reflectances of the ZnO nanowire samples which could be compared to a silicon substrate.

For measurements with the Lambda 950 spectrometer, the ZnO nanowire sample was placed at the back of the sphere at a standard angle of 8^{o} incidence. The internal surfaces of the sphere were coated with Spectralon ®, which has a diffuse reflectance of 0.99 for light 400 nm -1100 nm. The integrating sphere was operated in the two-bream mode with a reference beam which helped eliminate substitution errors arising from the placement of the samples. Reflected light from the sample was diffusely reflected around the sphere. As the ZnO nanowire samples were smaller than the 25 mm diameter reflectance port, a sample holder was made with a circular aperture of 13mm. The sample

holder caused an offset in the measured reflectance, which will be addressed in the results section.

The second integrating sphere was attached to a Fluorolog III spectrometer, commonly used for fluorescence measurements. The Fluorolog III integrating sphere allowed reflectance measurements at different angles of incidence thereby providing insight into the angular dependence of the sample reflectance. The sphere was 4 inches in diameter with a center mount sample holder that could be placed at different angles with respect to the incident beam. The sample holder allowed for a sample 12 mm by 12 mm. in dimension. Figure 13 shows images of the sphere and sample holder.

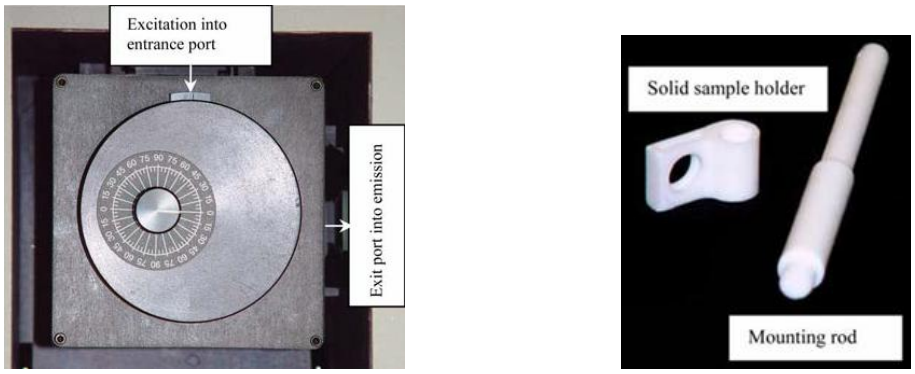

(a) **(b)**

Figure 13. (a) Configuration of Fluorolog III - 4 inch integrating sphere. Sample is mounted in the center mount below the angular control. (b) Solid sample holder used for nanowire samples [43].

The geometry of the sphere allowed for sample reflectance measurements at the incident angles ranging from 15^{o} to 40^{o}. At angles smaller than 15^{o}, light reflected by the sample was directed towards the detector. At angles greater than 40^{o}, incident light hit the sample holder. A background scan was taken with the sample in the sphere but with the light source not hitting the sample. While this background scan eliminated substitution errors caused be placing the sample inside the sphere, the measurements were not as reliable as those made with a sphere operating in the two-beam mode [44].

Measurements using the Fluorolog III were taken in Real Time Control (RTC) mode by setting the light emission beam and detector to the same frequency of light. This method was more efficient than using the software for fluorescence scans as the samples were not expected to fluoresce at visible wavelengths. Measurements were taken manually by inserting a ZnO sample, turning the sample at 5^{o} increments, and recording the counts. The measurements were performed at set wavelengths from 300 nm to 800 nm and at angles from 15^{o} to 60^{o}.

3. Results and Discussion

ZnO nanowires were grown using two different methods, aqueous chemical growth (ACG) and electrodeposition. All wires exhibited *c*-axis, hexagonal crystal growth, however, nanowire array morphology depended on the growth method. ACG grown nanowires exhibited vertical orientation while electrodeposited nanowires tended to have a random orientation. The use of a planar ZnO layer as a seeding layer affected nanowire morphology for both deposition methods. A wide range of morphologies was explored. Optimization of growth was focused on creating AR coatings. According to theory, these should have long, thin nanowires, with substantial height variations. ACG is a more versatile method than electrodeposition since it can be performed on both conductive and non-conductive substrates. In addition, the morphology of the wires grown using ACG showed greater promise as an optimum AR coating. Thus, more attention went toward developing the ACG method experimentally. Appendix 1 lists the properties of all ZnO nanowires samples grown.

3.1 SEM images and Analysis of ZnO Nanowire Morphology

Scanning Electron Microscope images were made of the samples grown by ACG and electrodeposition. The images were used to evaluate the average ZnO nanowire lengths, diameters, and number density for each growth. Images also provided information about the orientation of the nanowires.

3.1.1 Aqueous Chemical Growth (ACG)

Wires grown by ACG tended to be orientated vertically. Initial trials indicated that the growth of ZnO nanowire arrays required a seed layer provided by the spray pyrolysis of zinc acetate. Optimal growth occurred in a steady state, covered bath. Figure 14 shows results from initial trials of 0.05 M, 0.02 M and 0.1 M concentrations. Without a seed layer, large crystals formed and there was no uniform nanowire growth. With a seed layer, stirring or moving the solution would result in large crystals deposited on nanowire arrays.

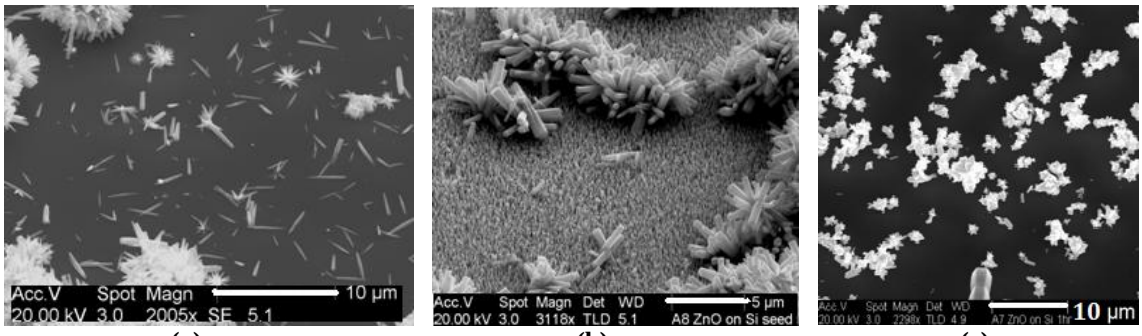

(a) **(b)** **(c)**

Figure 14. Initial attempts to grow uniform ZnO nanowire arrays by ACG. (a) Sample A1: 0.05 M. No seed layer. (b) Sample A8: 0.02 M. Large ZnO crystals deposited on wires due to stirring solution. (c) Sample A7: 0.1 M. No seed layer.

The seeding layer was created by spray pyrolysis of zinc acetate. The seed layer acts as a nucleation site for the polar growth of the ZnO nanowires. Figure 15 shows the various numbers of layers that were used to seed the silicon substrate. Uniform nanowire growth took place using 5, 10, 20 and 40 spray layers. Nanowire height varied from 200 nm to 1100 nm, with a diameter range of 32 nm to 120 nm.

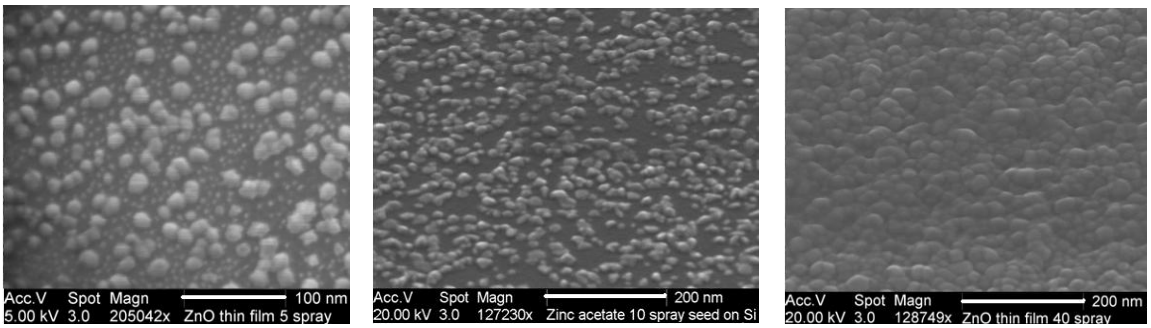

(a) (b) (c)

Figure. 15. (a) 5 Spray layers of zinc acetate leave ZnO "seeds" on Si. The seeds average 15 nm in diameter. (b) 10 spray layers of zinc acetate leads to seeds with an average diameter of 20 nm. (c) 40 spray layers of zinc acetate leads to a planar ZnO surface estimated to be between 40 nm – 60 nm in thickness.

Regardless of the seeding layer, samples with uniform vertical nanowire growth appeared visually opaque when deposited on the silicon surface. Examples of uniform nanowires grown by ACG are shown in Figure 16.

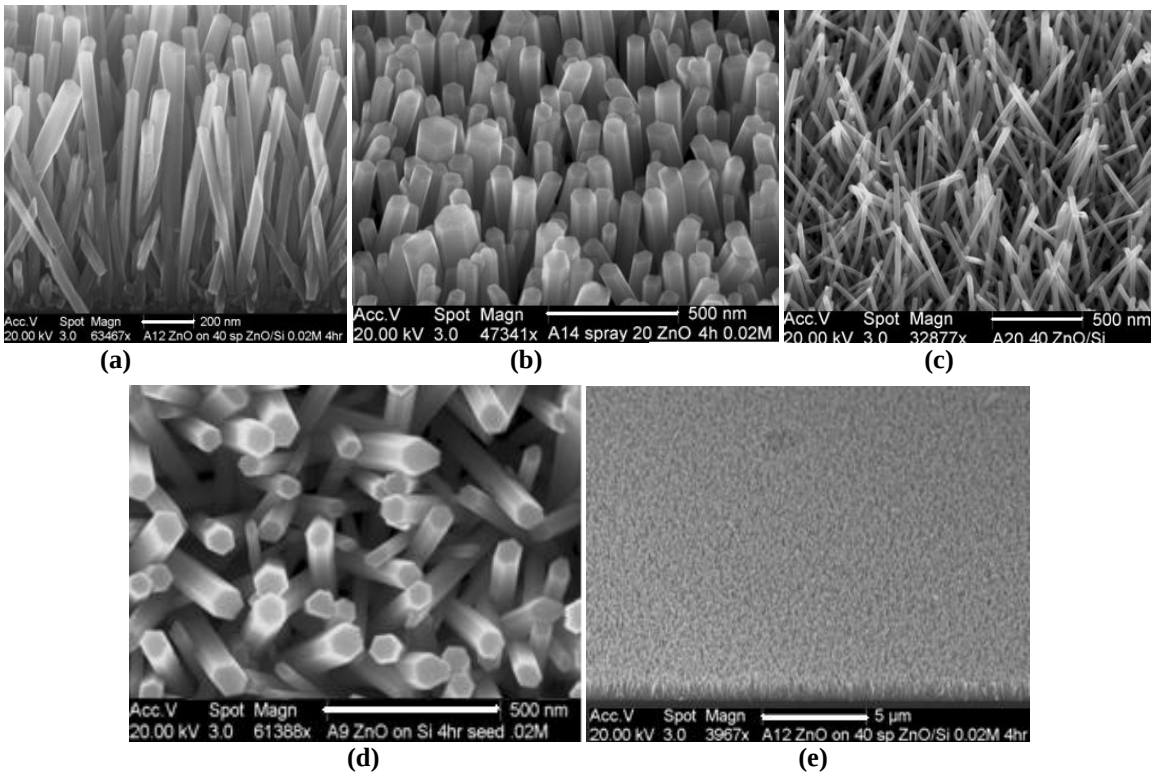

(a) (b) (c)

(d) (e)

Figure 16. (a) Side view of 0.02 M vertical wires (Sample A12). (b) 30^{o} tilted view of nanowire density (Sample A14). (c) 0.01 M nanowire growth (Sample A22) (d) Top view of nanowire hexagonal faces (Sample A9) (e) Uniformity of sample growth (Sample A12).

Table 2 summarizes the properties of ACG nanowires evaluated from SEM images. The average length and diameter were found by averaging 7 to 10 nanowires. The standard deviation of the diameters was 20 nm to 30 nm. The length was difficult to assess from the images because of dense nanowire growth, and had a greater deviation of 100 nm to 200 nm. The fractional area is the product of the number of nanowires per unit area and the average cross-sectional area of the wire. Appendix 1 lists all samples grown by ACG.

Table 2: Uniform ZnO Nanowires Grown on Silicon by ACG

No.	Sample ID	Pre-growth (Sprays of Zinc acetate)	Avg. Length (nm)	Avg. Diameter (nm)	Number Density (Wires/μm^2)	Fractional surface area	Notes:
1	A9	20 sprays	1100	94	62	0.430	0.02 M/ 4hr
2	A10	10 sprays	900	120	32	0.362	0.02 M/ 4hr
3	A11	5 sprays	X	48	170	0.307	0.02 M/ 4hr
4	A12	40 sprays	960	68	90	0.327	0.02 M/ 4hr (95C)
5	A13	40 sprays	X	80	54	0.271	0.02 M / 4hr
6	A14	20 sprays	950	90	67	0.426	0.02 M/ 4hr
7	A15	10 sprays	845	56	86	0.211	0.02 M/ 4hr
8	A16	40 sprays	1060	100	43	0.338	0.02 M/ 4hr
9	A19	40 sprays	900	63	65	0.203	0.02 M/ 4hr
10	A20	40 sprays	418	32	190	0.153	0.01M/ 5hr
11	A22	40 sprays/ 50 nm TiO_2	1070	110	20	0.190	0.02 M/ 4hr

The seeding layer affected the morphology and density of nanowire growth; however, the relationship between the layer and nanowire density was unclear. Uncontrollable variation in the spray pyrolysis method led to an indeterminate relationship between nanowire growth and the seed layer. A 40 spray layer was found to produce the most dependable growth. The 40 layers provided a uniform ZnO planar surface estimated to be 40 nm – 50 nm thick. A planar layer between the nanowires and

the silicon provides the best match for a gradient-index optical coating made of ZnO nanowires.

The ZnO nanowires arrays showed a clear relationship between growth density, nanowire diameter, and nanowire length as shown in Figure 17.

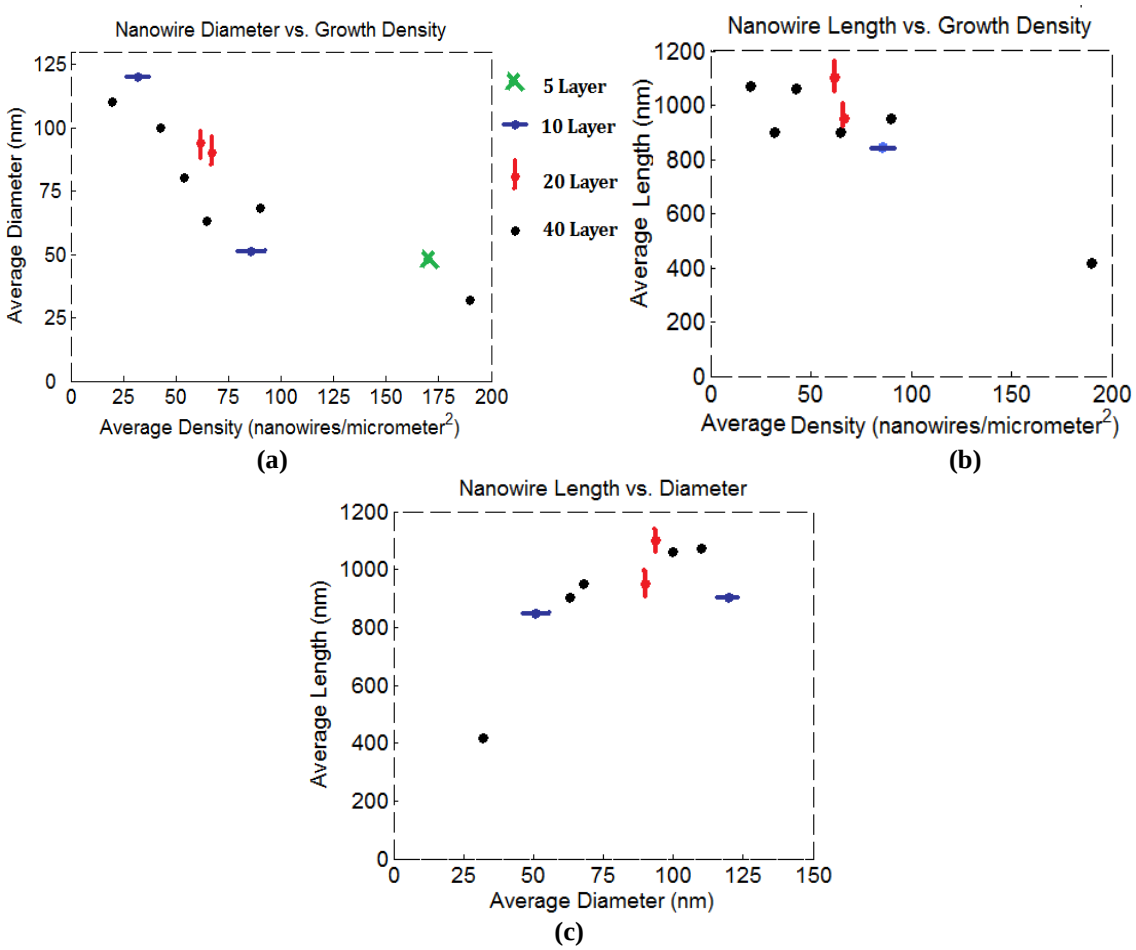

Figure 17. ACG growth results. Different symbols indicate the number of zinc acetate layers used to seed the substrate. (a) Nanowire diameter and growth density. (b) Nanowire length and growth density and (c) Nanowire length and diameter.

As nanowires increased in diameter they decreased in number density. No other correlations were obvious between the diameter, length, number density, and the fraction of surface area coved by the nanowires. ZnO nanowires grown in a 0.02 M bath had

vertical alignment, with vertical tilt less than15°. Nanowires grown at 0.01 M concentration had vertical tilts less than 30°.

3.1.2 Electrodeposition

ZnO nanowires grown by electrodeposition tended to be randomly orientated. Their vertical tilt could extend to 80°. They were also longer and had larger diameters than those grown by aqueous bath. Wires were initially grown on ITO covered quartz to determine the optimum conditions for growth. Figure 18 shows examples of nanowires on ITO/quartz.

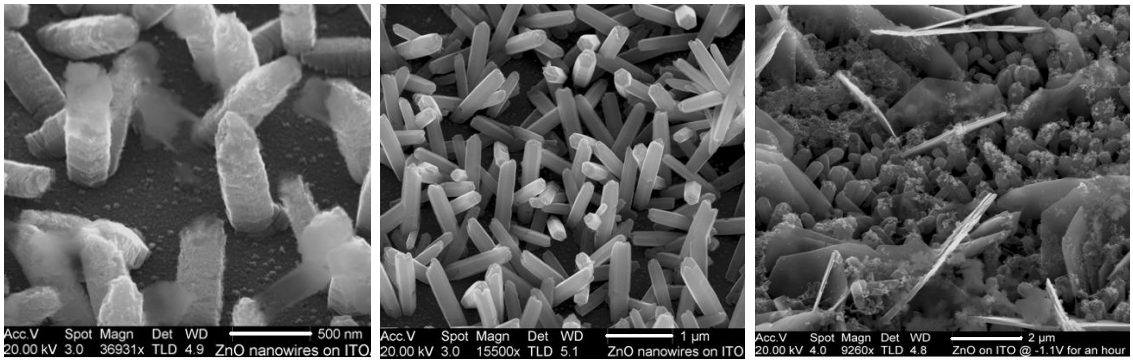

(a) **(b)** **(c)**

Figure 18. ZnO nanowires grown by electrodeposition on ITO/Glass, with the relative voltage of the cathode at: (a) Sample G1: -1.00V (b) Sample G2: -1.05V and (c) Sample G3: -1.10V.

Table 3 lists the nanowire lengths, diameters and number densities.

Table 3. Electrodeposited ZnO Nanowires on ITO/Quartz

No.	Sample ID	Voltage (V)	Avg. Length (nm)	Avg. Diameter (nm)	Density (Wires/µm^2)
1	G1	- 1.00	700	225	0.72
2	G2	- 1.05	1000	250	4.44
3	G3	- 1.10	NA	NA	Platelets

For AR coatings, the best density and length of ZnO nanowires were produced by electrodeposition at a potential difference of -1.05 V. After trials on ITO/quartz, electrodeposition was then used to grow nanowires on ITO/silicon substrates.

Three different samples were prepared on ITO/silicon, two without a seeding layer and one with a planar ZnO layer created by spray pyrolysis. Sample I1 was grown directly on ITO/Si with a potential of -1.05 V, and is shown in Figure 19.

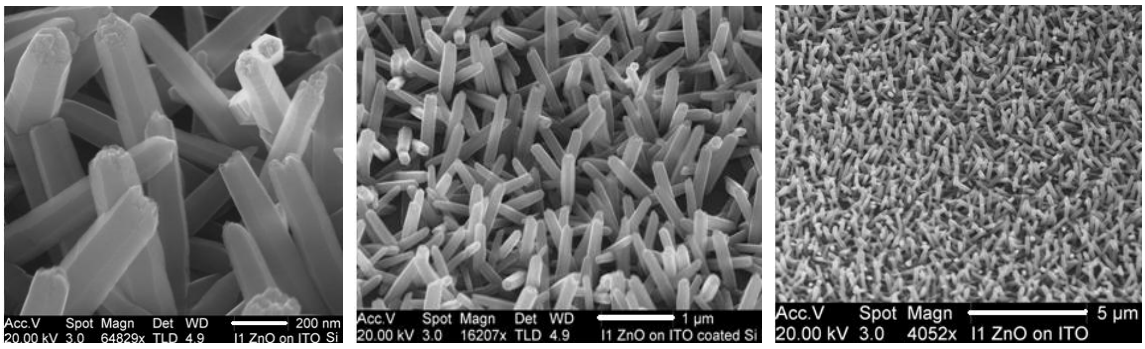

(a) **(b)** **(c)**

Figure 19. Sample I1: ZnO deposited at -1.05 V on ITO/SI with scale bars (a) 200 nm (b) 1 µm and (c) 5 µm.

The ZnO nanowires have diameters of 150 nm to 200 nm and lengths of roughly 1 µm. These wires have similar dimensions as those grown on ITO/quartz. Sample I3 was grown with the same growth conditions, but could have had anomalous electrical contact with the substrate. The ZnO nanowires of Sample I3 exhibited a flower like morphology as shown in Figure 20.

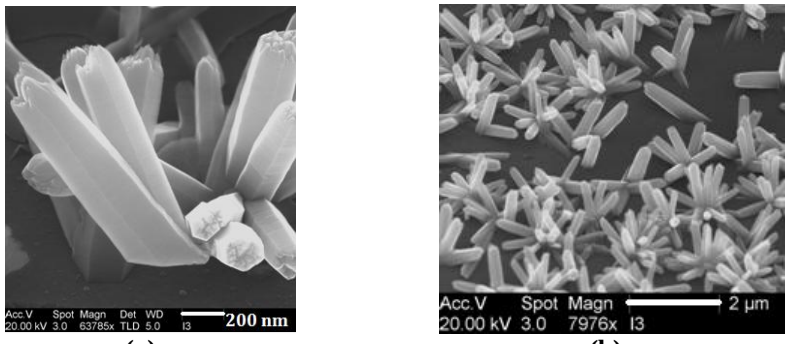

(a) **(b)**

Figure 20. Sample I3: ZnO deposited at -1.05 V on ITO/SI with scale bars (a) 200 nm (b) 2 µm.

The third sample grown by electrodeposition was grown on a planar layer of ZnO deposited by spray pyrolysis on ITO/silicon. The planar layer created a dense array of

nanowires with dimensions comparable to those of the vertical ZnO nanowires grown by ACG. Figure 21 shows sample I2, which had average diameters of 85 nm and average lengths of 500 nm.

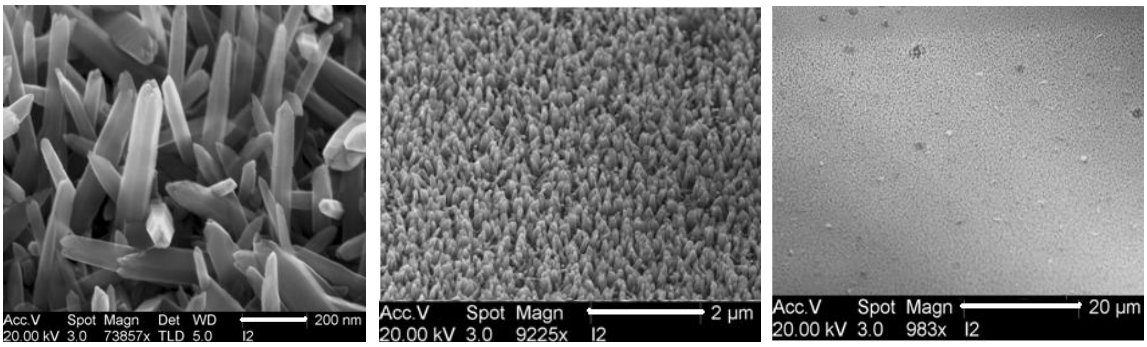

(a) **(b)** **(c)**

Figure 21. Sample I2: ZnO deposited at -1.05 V on planar ZnO on ITO/SI with scale bars (a) 200 nm (b) 2 µm and (c) 20 µm.

Table 4 lists the dimensions and morphology of ZnO nanowires deposited by electrodeposition on ITO/Si.

Table 4. Electrodeposited ZnO Nanowires on ITO/Si at -1.05 V

No.	Sample ID	Pre-growth (Sprays of Zinc acetate)	Avg. Length (nm)	Avg. Diameter (nm)	Density (Wires/μm^2)	Fractional surface area	Visual
1	I1	None	1050	180	5.5	0.140	White
2	I2	40 sprays	500	85	30	0.170	Opaque
3	I3	None	850	200	5 (Flowers)	0.157	White

The samples differed visually. The samples with larger wires and smaller number densities appeared white on the ITO/Si surface, whereas the dense nanowire sample I2, appeared as an opaque layer. All wires exhibited a hexagonal shape with random orientations and variations in length and diameter. Although they differed in length and diameter, the fractional area covered by nanowires was similar for all samples, and generally less than the fractional area covered by ACG wires.

3.2 Goniometer

3.2.1 Introduction to Measurements

The goniometer was used to measure the diffuse and specular reflectivities for the ZnO nanowire samples. These reflectivities were compared with the reflectivity of silicon. Random and systematic errors for goniometer measurements made them primarily useful for qualitative comparisons.

The 532 nm diode laser required a 1 hour warm-up to reach constant power. Following this warm-up, the laser output varied 2-3% during the scan. The lock-in amplifier had difficulty measuring the weak diffusely reflected radiances from the samples. A signal level below 5×10^{-12}A was generally considered to be in the noise. Currents 5×10^{-12}A and below appeared to vary randomly. At the other extreme, samples with high specular reflectivity often overloaded the lock-in amplifier, requiring attenuation of the signal with resistors and neutral density filters.

The most common source of measurement error was the alignment of the samples with respect to the laser and photodiode. A beam splitter or mirror was used to reflect scattered laser light from the sample into the photodiode. If the sample made a slight vertical tilt in the sample holder ($<1^{o}$) the specular peak would not be measured accurately. For diffusely reflecting samples, it was difficult to identify the specular reflection peak, leading to error in alignment and measurement. For specular reflecting samples, small movements, such as the vertical tilt mentioned above, could cause >10% errors in the reflectivity.

The following alignment procedure was used for the goniometer. First, the laser was aligned in the horizontal plane. Second, the two stepper motors that controlled the photodiode arm and the sample stage, respectively, were calibrated in angle increments around a circle. Last, the sample was placed in the sample holder and positioned normal to the laser in both the vertical and horizontal plane by using the specular reflection of the laser's beam. Even with thorough calibration, systematic errors could be introduced through the scattering of light by the sample holder and the edges of the beam slitter. For these reasons, multiple scans were taken for each sample in order to verify the repeatability of measurements.

Despite the sources of error, the precision of the multiple scan measurements was high, provided the sample was not moved. This precision is illustrated in Figure 22a. If the sample was moved, slight changes in the sample surface and alignment contributed to different results, as seen in Figure 22b.

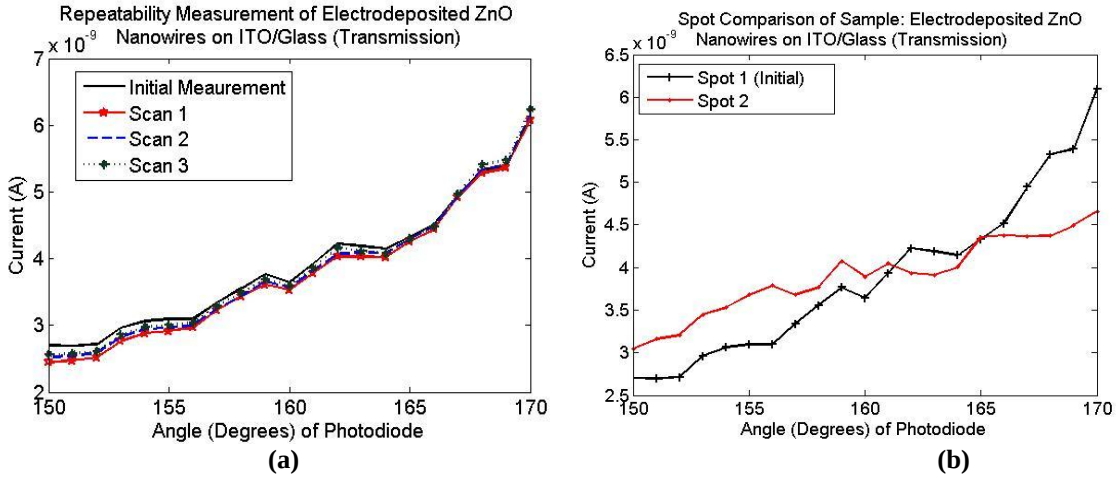

Figure 22. Repeatability of goniometer measurements for electrodeposited ZnO nanowires on ITO/quartz glass: (a) precision of spot repeatability and (b) difference caused by moving the sample.

Owing to the variability caused by alignment, the drift of laser power over time, and the need to introduce filtering, the goniometer scans were used primarily for qualitative comparisons.

3.2.2 Scatter Scan

A scatter scan of reflected light was performed by illuminating the sample with the laser at normal incidence, and rotating the photodiode at 1^o increments in the horizontal plane. The angles were measured with respect to normal incident light at 0^o. To measure the reflectivity, light was reflected from the sample by a beam splitter or silicon mirror. While measuring reflectivity at normal incidence, the glass beam splitter interfered with the laser beam, thereby reducing the specular reflection peak. For a silicon mirror, the sample was turned 2^o with respect to normal in order to measure the specular reflection at 4^o. Measurements taken with a small angle offset were plotted with respect to normal incident light in order to qualitatively compare samples. The current was used for scatter scan plots as it was proportional to the irradiance of the photodiode and thus to the reflectivity.

Measurements showed that vertically oriented ZnO nanowires grown by ACG exhibited diffuse reflection, with a specular reflection peak below that of silicon, as presented in Figure 23. ACG samples A9, A12, and A15, shown in Figure 23, had diameters of 65 nm to 90 nm. Repeatability measurements and scans on different parts of the same samples are shown in Figure 24. The results illustrate the consistency of the signal and the dependence of the reflectivity on the sample surface and alignment.

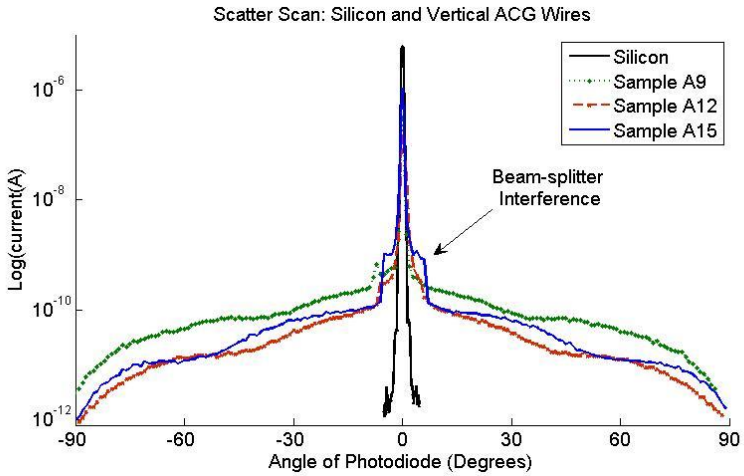

Figure 23. Scatter scan for ACG ZnO nanowires grown using a 4 hr 0.02 M bath. Measurements were performed with a glass beam splitter.

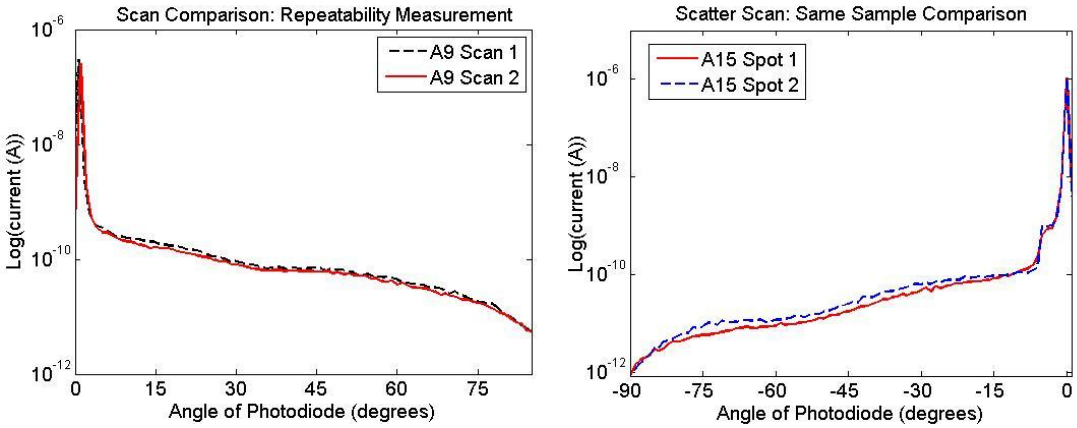

(a) **(b)**

Figure 24. Reflectivities at normal incidence using a glass beam-splitter (a) Repeatability measurement of sample A9 without moving sample. (b) Comparison of reflectivities for sample A15 where the sample was moved in between measurements.

The scattering by the ACG vertical nanowire samples is not Lambertian, and is characteristic of the vertical orientation and size of the nanowires. In contrast, samples that had large crystal growth, such as sample A8 shown in Figure 14b, exhibited Lambertian scattering. The reflectivity was proportional to cos(θ) function, where θ is the angle from the normal.

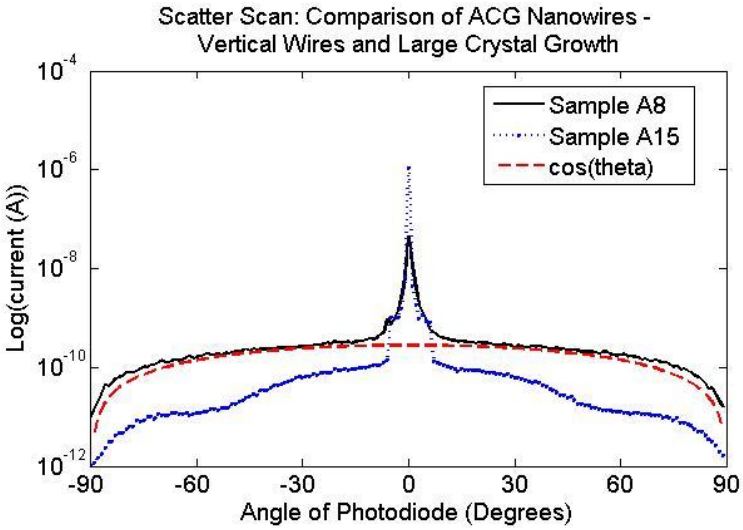

Figure 25. Comparison of the Lambertian scattering for sample A8 with large crystal growth of sample A8 to the reduced diffusivity for sample A15 with no crystal growth.

Figure 25 shows cos(θ) compared to the reflectivity for vertical nanowires with and without large crystal growth. The specular reflection peak for sample A8 was not accounted for by Lambertian scattering.

Randomly oriented ZnO nanowires grown by electrodeposition showed diffuse reflectivity similar to that caused by the large crystal growth on sample A8. Figure 26 compares the reflectivity of randomly oriented nanowires to the reflectivity of silicon. Most randomly oriented nanowires exhibited Lambertian reflectivity and a smaller specular reflectivity. Nanowire dimension and orientation may contribute to diffuse scattering. Sample I1 had a diameter of 185 nm, which was less than the 500 nm diameter of the large crystal growths, but greater than the diameters of the vertical ZnO nanowires.

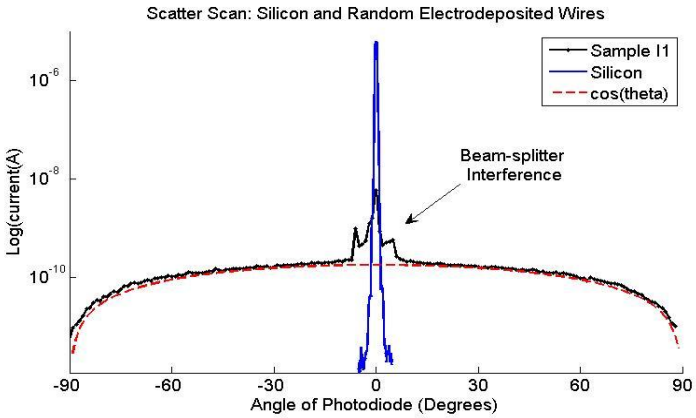

Figure 26. Lambertian fit of Sample I1, randomly oriented ZnO nanowires grown by electrodeposition.

Compared with randomly oriented nanowires with larger sizes, sample I2 exhibited strong specular reflection and smaller diffuse reflectivity. Sample I2, grown by electrodeposition on a planar ZnO layer, had randomly oriented nanowires and average diameters of 85 nm, which were within the range of the diameters of the vertical nanowires. Figure 27a compares the scattered light for samples I1and I2. Compared with vertical nanowire samples having a similar nanowire diameters, sample I2 had larger diffuse reflectivity and smaller specular reflectivity, as shown in Figure 27b.

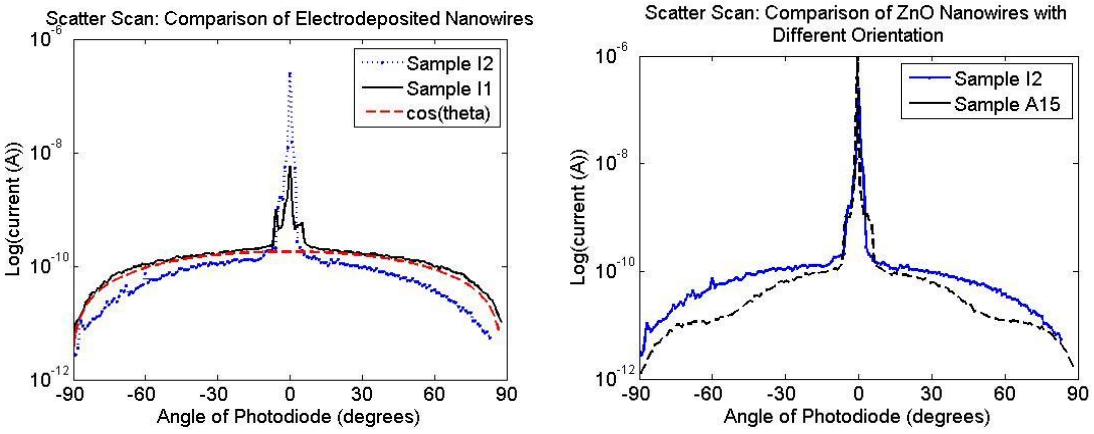

(a) **(b)**

Figure 27. (a) Reflectivity of randomly orientated nanowires with large diameter (I1) and small diameter (I2). Only I1 showed Lambertian scattering. (b) Reflectivity for nanowires with different orientations but similar diameters. Sample I2 had randomly oriented nanowires and sample A15 had vertically oriented nanowires.

Reflectivity data collected with goniometer scatter scans was integrated for normal incident light, assuming symmetry about the incident beam, to yield the total power of the scattered light. The integrations depended on accurate measurements of the specular peak, and samples with large specular reflectivities were measured with angular steps of 0.1°. Errors of up to 11% in the total reflectance were unavoidable due to variations in amplitude caused by sample alignment. The integration of the current gave the total current over a hemisphere: $I_{total} = \sum \frac{I(\theta_i)}{L^2} \cdot \alpha_i \cdot \frac{2\pi R sin(\theta_i)}{2} \cdot R d\theta$, where $I(\theta_i)$ is the measured current, *R* is the radius at which the photodiode moves around the sample, and θ_i is the angle that the detector makes with the normal to the sample. Figure 28 shows the geometry used for integration.

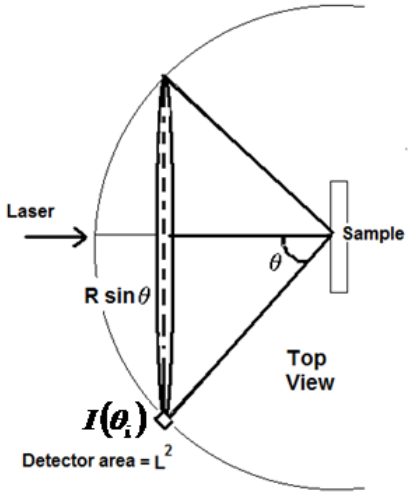

Figure 28. Top view of the geometry for goniometer integration

To account for the variations in the angular increment required for accurate integration, the increment $\Delta\theta = \frac{L}{R}$, where *L* is the width of the detector, was adjusted by a factor α_i. Measurements of samples were taken at 1° angle increments so that $\alpha_i \approx 1$. Silicon and the incident beam, however, had large peaks of intensity for θ = 0°. These peaks were

measured at smaller increments, $\alpha_i \approx 0.1$. Integration of the current was over a hemisphere. The current was multiplied by a factor $\alpha_i 2\pi R sin(\theta) R d\theta$. The area of the detector was taken into consideration by dividing the measured current, I_i, by the area of the detector, L^2. The integration was for θ_i ranging from -90° to 90°. Since measurements were taken to be identical on both sides of the incident beam, the average value of the two measurements was used. The total was thus divided by a factor two. The total current is given by: $I_{total} = \sum \frac{I}{L} \alpha \cdot \Delta\theta \cdot \pi R sin(\theta)$. The same integration was performed for the incident beam. Unfortunately, large percent uncertainties arose from the errors in the amplitudes of the specular peaks caused by misalignment of the sample.

Table 5: Goniometer: Total Integrated Currents and Reflectances

Sample	**Total Integrated Current +/- 11%**	**Reflectance +/- 15%**
Silicon	3.42×10^{-6} A	33%
Sample A12	7.29×10^{-7} A	7%
Sample A13	6.83×10^{-7} A	7%
Sample I1	2.36×10^{-6} A	23%
Incident beam*	1.05×10^{-5} A	

*Integrated current of 532 nm laser beam measured at 180° with no sample in holder

All nanowire samples had reflectances less than that for silicon. Large, diffusely reflecting nanowires such as sample I1, had a greater reflectances than the smaller, vertical nanowire samples. The vertically oriented nanowire samples A12 and A13 had the smallest reflectances. The results of the integrations indicated the relative reflectances of the nanowire samples. Owing to the difficulty of measuring the specular peaks, the reflectances of the samples may be artificially low. Consequently, an integrating sphere was used to verify the total reflectances for the nanowire samples. Section 3.3 discusses the integrating sphere results. Although measurements by the goniometer were uncertain,

they provided an advantage over an integrating sphere by differentiating between specular and diffuse reflectivity. By using the goniometer, the type of scattering which was measured for each sample could be associated with the nanowire morphology.

Scatter scans of the ZnO nanowires were also performed with the sample at oblique angles to the incidence light. However, turning the sample with respect to the incident light ruined the symmetry about the axis of the incident laser beam. Therefore, conclusions about the total reflection of the sample as a function of angle could not be made. Alternatively, angular measurements were taken of the specular reflection peak as a function of angle.

3.2.2 Angle Dependent Specular Reflectivity

The angle dependent specular reflectivity was measured for the ZnO nanowires using the goniometer specular scan program. The goniometer sample holder turned at 0.5^{o} increments to the incident laser beam, while the photodiode tracked the specular reflection peak by positioning itself automatically at twice the angle of incident light.

In the specular scan measurement, a variable linear polarizer was placed in front of the laser beam chopper, along with a filter to attenuate the signal. A silicon mirror was used in place of a glass beam splitter to reduce noise. Alignment of the sample and photodiode was critical for consistent measurement of the specular peak. Alignments were performed between each scan. Specular reflectivities of the sample were measured from 0^{o} to 83^{o} for TE and TM polarized light.

The difficulty of the alignment for the specular scans led to fewer samples being measured. Figure 29 shows the specular reflectivity of silicon which fits the theory for an index of refraction n = 3.95. The reflectivity of the silicon at 4^o was used to normalize the measurements to the theoretical values. The amplitude of the measured current from 0^o to 83^o was divided by the amplitude of the current measured at 4^o, then multiplied by the theoretical reflectivity for normal incidence. Normalization of the measured silicon reflectivity at near-normal incidence allowed the TE and TM polarized reflectivities to be compared to the theoretical values.

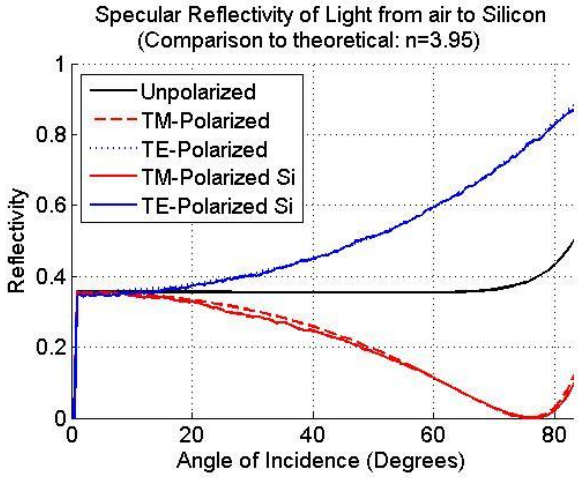

Figure 29. Specular reflection for silicon normalized to a theoretical reflection for a material with index of refraction *n*=3.95. The experimental reflectivity for TE polarized light covers the theoretical value.

The index of refraction used for the theoretical fit was the value which best fit the measured reflectivities for both the TE and TM polarized waves. Although the reflectivity of the laser with a nominal wavelength of 532 nm indicates a larger index of refraction for silicon, n = 4.2 [2], this discrepancy might be attributed to the laser calibration and alignment errors. In addition, reflection by the silicon mirror used to direct light from the sample into the photodiode might also have cause aberrations in the

polarization. Despite the discrepancies, a qualitative comparison could be made between the specular reflectivities for silicon and those for ZnO nanowire arrays.

Specular reflection measurements were performed for vertical nanowire sample A15 and randomly oriented nanowire samples I1 and I2. The samples were normalized using the same factors used for silicon normalization. Measurements were taken multiple times to verify their amplitudes.

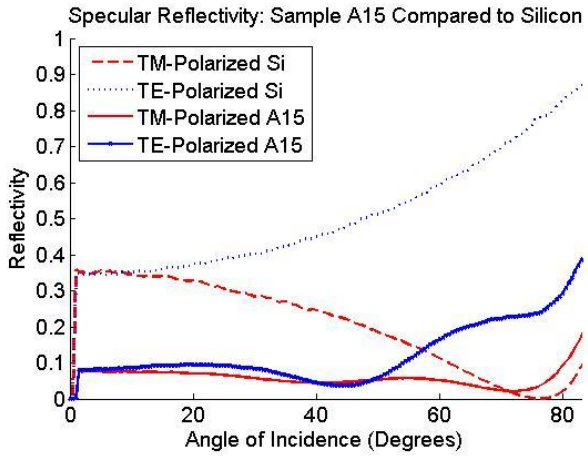

Figure 30. Specular reflectivity for polarized light for silicon and sample A15, vertical nanowires, with a diameter of 51 nm. Values were experimentally found and were normalized with the same coefficients used for silicon normalization.

Figure 30 shows the polarization dependence of the specular reflectivity for vertical ZnO nanowires. Scatter scans of the vertical nanowires had shown high specular reflection peak and low diffuse reflection. Although significantly less than the specular reflectivities of silicon, the nanowire reflectivities still exhibited polarization dependence.

Compared with vertical nanowire samples, samples I1 and I2 with randomly oriented ZnO nanowires had much smaller specular reflectivities with little variability in the reflection for TE and TM polarized light. Figure 31 shows the specular reflectivities for electrodeposited samples and silicon. Sample I1, with average nanowire diameters of 180 nm, showed nearly identical specular reflectivities for TE and TM polarized light.

The reflectivities were much smaller than those for silicon, except when approaching grazing angles of incidence. Sample I2, with average nanowire diameters of 85 nm, showed polarization dependent specular reflectivities at angles greater than 40^{o}.

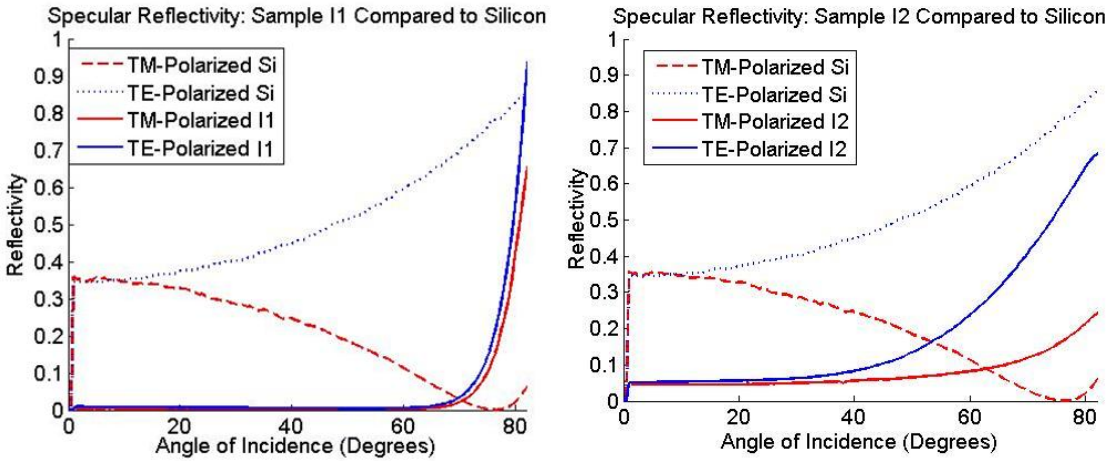

(a) **(b)**

Figure 31. Specular reflection of polarized light compared to that of silicon for (a) Sample I1, randomly oriented nanowires with a diameter of 180 nm (b) Sample I2,vrandomly oriented nanowires with a diameter of 85 nm. Values were determined experimentally and normalized to those for silicon.

The differences in specular reflectivity might be characteristic of the sizes of the nanowires. Indeed, the smaller nanowires of Sample I2 showed a specular reflectivities similar to those of vertical nanowires with similar diameters. At large angles of incidence, all nanowire samples had sharp increases in specular reflectivities, with the largest increase for highly diffuse reflecting samples. Section 3.3.2 discusses the total reflectance of the nanowire samples as a function of angle using an integrating sphere.

3.3 Integrating Sphere

Two integrating spheres were used to perform total reflectance measurements, a 150 mm integrating sphere attached to a Perkin Elmer Lambda 950 UV/VIS/NIR spectrometer, and a 4 inch integrating sphere attached to a Horiba Jobin Yvon

Fluorolog III spectrometer. The Lambda 950 integrating sphere was larger and operated in two-beam reflectance mode. It thus provided better total reflectance measurements. The Fluorolog III integrating sphere was capable of performing angle dependent total reflectance measurements but had a geometry that might have caused quantitative errors. The Fluorolog III measurements were used to make qualitative comparisons of the reflectances for the ZnO nanowire arrays at oblique angles of incidence.

3.3.1 Introduction to Total Reflectance Measurements

Total reflectance measurements of the ZnO nanowire samples were performed with the samples at the reflectance port of the Lambda 950 integrating sphere. The port was located at the back of the sphere at 8^{o} incidence to the light source. The sample port, 25 mm in diameter, was larger than most of the ZnO nanowire samples. To center them in the port, the samples were place behind a holder with a 13 mm diameter hole. Figure 32 shows the configuration for the Lambda 950. The holder was made from aluminum and painted with white acrylic paint. Samples measured using the Fluorolog III were 12 mm squares. For measurements in the Lamda 950, these samples required a modified sample holder. White vinyl electrical was used to cover the additional area in the aperture of the sample holder.

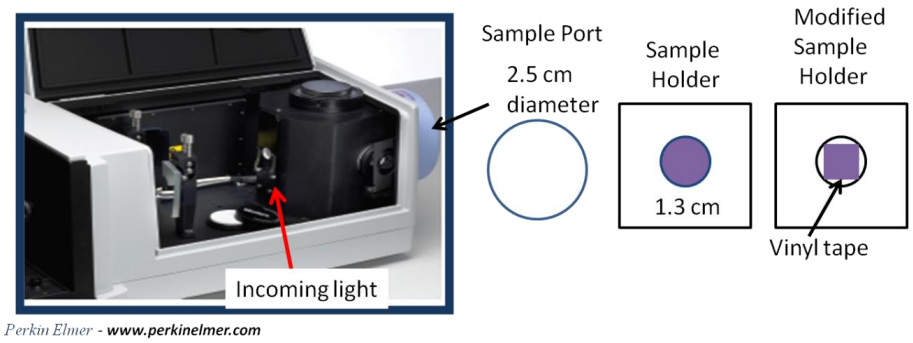

Figure 32. Configuration of the Lambda 950 Integrating sphere showing the reflectance sample port, sample holder for small samples, and modified sample holder used for the 12 mm square samples. The coloring shows how the was sample mounted behind the holder before being placed in the reflectance sample port.

Integrating sphere measurements should not be performed with sample holders as they alter the total reflectance of the sphere. The holders might also contribute to the light initially reflected by the sample. On the other hand, the small sample sizes were advantageous for their relatively small cost, and the ease of characterization measurements.

An adjustment was determined to compensate for the contribution to the total reflectance by the sample holder. Adjustments depended on the change in the average reflectance of the integrating sphere and the contribution to the initial reflection by the sample holder. Although the adjustment parameters could not be independently determined they were obtained by comparing experimental data collected with the holder and data collected without the holder.

In an integrating sphere, the radiance, L, from an incident fluxφ_i, on a surface of reflectivity ρ, is given by $L = \frac{\varphi_i \rho}{\pi A}$ $(w/m^2/sr)$, where π is the projected solid angle, and A is the illuminated area. By radiative transfer, the amount of radiant flux an area receives is proportional to the fraction it occupies in the sphere's surface area. Assuming diffuse

reflection, and equal radiation from each point, multiple reflections increase the total flux. Taking into account these multiple reflections and the port openings, the total radiance of the sphere , L_s, is given by: $L_s = \frac{\varphi_i}{\pi A_s} \cdot M$, where A_s is the surface area of the sphere and M is referred to as the sphere multiplier. The sphere multiplier depends on the initial reflectance of light ρ_o and the average sphere reflectance $\bar{\rho}$ and is given by $M = \frac{\rho_o}{1-\bar{\rho}}$. The average sphere reflectance depends on the reflectivity of the sphere wall, the fractional area of the port openings, and the reflectivity of the ports. The reflectivity of the sphere, ρ_{sphere} is calculated from the ratio of the measured sphere radiance to the radiance of a sphere coated with a reference standard, L_s. The reflectance is given $\rho_{sphere} = \frac{L_s}{L_r} \cdot \rho_r$, where ρ_r is the reflectivity of the reference standard [42]. The reference standard used was Spectralon©.

The sample holder altered the average reflectance of the sphere and reflected a fraction of the incident light. The integrating sphere software controlled the slit width, and would adjust it to maintain an optimal irradiance for the light detector. As a result, light was incident not only on the nanowire sample but also on the white metal plate. The radiance of the sphere thus depended on the reflectivity of the sample holder and the sample:

$$L_s = \left(\frac{\varphi_{sample}}{\pi A_s} \cdot \frac{\rho_{sample}}{1 - \bar{\rho}_{modified}}\right) + \left(\frac{\varphi_{holder}}{\pi A_s} \cdot \frac{\rho_{holder}}{1 - \bar{\rho}_{modified}}\right)$$

The fluxes were $\varphi_{sample} = \varphi_i f$ and $\varphi_{holder} = \varphi_i(1 - f)$. Here f represents the fraction of the area of incident flux hitting the sample, and $(1 - f)$ the fractional area occupied by the sample holder. The above modified equation for the radiance was introduced into the

equation used to find the reflectance of the sphere. The reflectance of the sample is given by:

$$\rho_{sample} = \rho_{sphere} \cdot \frac{L_r}{\rho_r} \cdot \frac{\pi A_s (1 - \bar{\rho}_{modified})}{\varphi_{sample}} - \frac{\varphi_{holder} \cdot \rho_{holder}}{\varphi_{sample}}$$

or $$\rho_{sample} = \rho_{sphere} \cdot \frac{L_r}{\rho_r} \cdot \frac{\pi A_s (1 - \bar{\rho}_{modified})}{\varphi_{if}} - \frac{(1-f) \cdot \rho_{holder}}{f}$$

Exact quantities of the variables were not known. In addition, variables were wavelength dependent. Nonetheless, the sample reflectance was given by: $\rho_{sample} = (\rho_{sphere}) \cdot \beta - \gamma$, where β and γ could be considered fitting parameters. The fitting parameters could be found experimentally by creating a linear fit between the sample reflectances measured with the sample holder to the reflectances measured without the sample holder. Three samples were used to find the fitting parameters for the sample holder. Reflectance spectra were taken for silicon, ITO/silicon, and sample A23, vertical ZnO nanowires grown by ACG. All three samples completely covered the reflectance port.

First, the reflectance of silicon and ITO/silicon were measured without the sample holder. They were compared with theoretical curves to assess the reasonableness of the calibration, as shown in Figure 33. The theoretical values were obtained using MATLAB using the wavelength dependent indices of refraction for intrinsic silicon [45] and ITO [46]. For silicon, the reflectances diverged from the theoretical values below 550 nm. Measurements, however, were consistent with other measurements of polished *n*-type silicon wafers. The reflectance of the ITO/silicon was obtained for a 27.5 nm layer of ITO on a silicon layer. The thickness of the ITO layer was optimized by a thin film

program in MATLAB. The thickness was consistent with the corresponding resistivity and transmittance of the ITO.

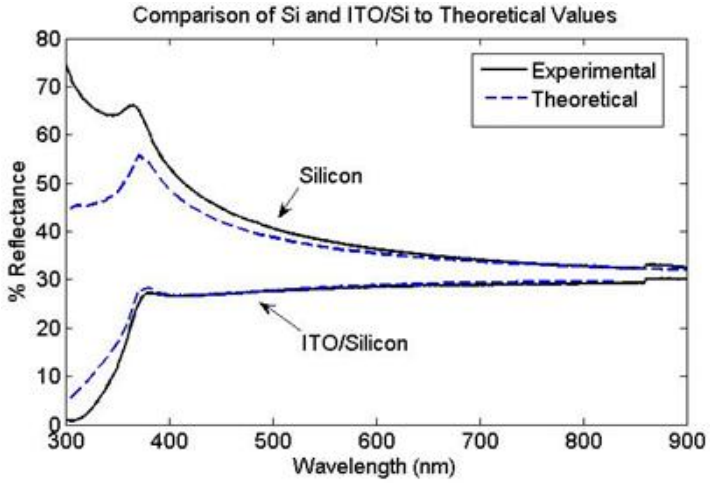

Figure 33. Measured and theoretical reflectances for silicon and ITO/Silicon. For ITO/Si a 27.5 nm layer of ITO was used.

Second, the reflectances for sample A23 were measured with the sample at the reflectance port of the integrating sphere. The sample holder was not used. Figure 34 compares the three reflectances. The band-gap of bulk ZnO was marked with a dotted line at 370 nm. ITO, which has a larger band gap of 3.7 eV, absorbed photons with wavelengths below 330 nm.

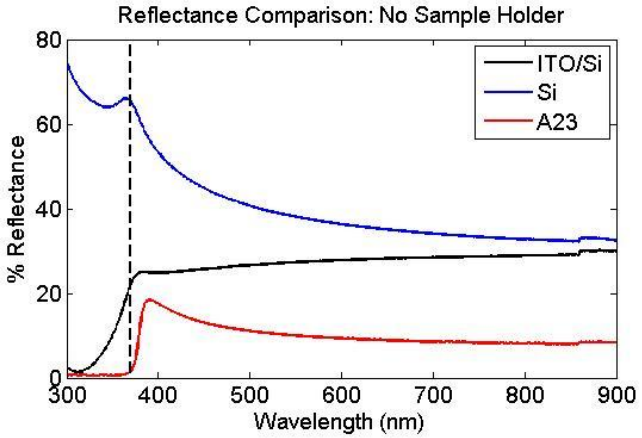

Figure 34. Reflectances of Silicon, ITO/Si, and vertical ZnO nanowire sample A23. All samples covered the reflectance port. The dotted line indicates the band-gap of ZnO.

Measurements preformed with the sample holder present had higher reflectances than without the sample holder, differing by roughly 4 percentage points, as shown in Figure 35a. Fitting parameters were found by a simultaneous linear fit of all three samples, shown in Figure 35b.

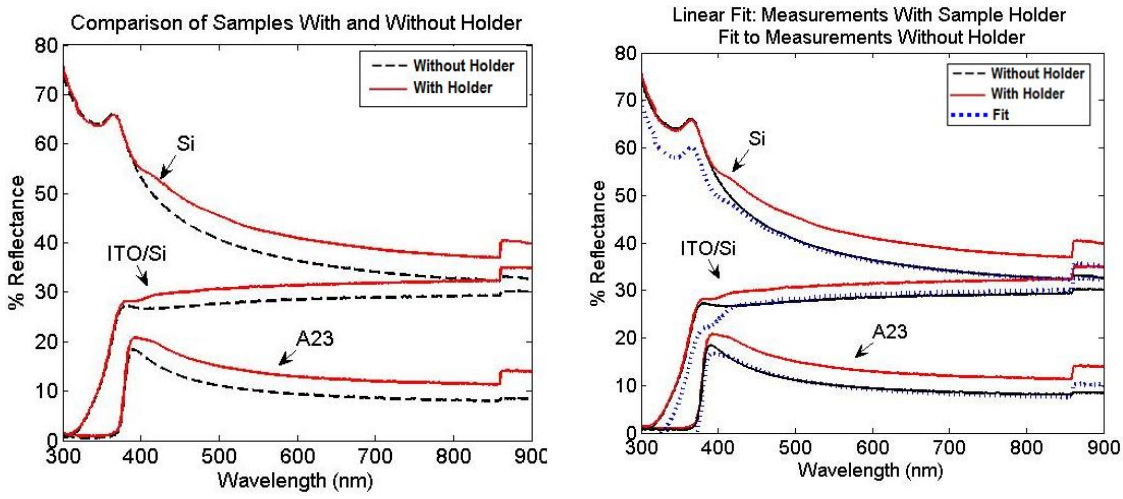

Figure 35. (a) Reflectances measured with and without sample holder for Si, ITO/Si, and A23. (b) Fit of reflectances to actual experimental values. β = 0.963 +/- 0.001; γ = 3.3 +/- 0.6.

The fit parameters were found to be $\rho_{sample} = (\rho_{sphere}) \cdot 0.963 - 3.3$. The values were found by a linear fit over the wavelength range from 400 nm to 860 nm. The R^2 was 0.998. Below 400 nm, the sample holder absorbed light. At 860 nm the detector changed from PbS to a photomultiplier tube (PMT), a filter changed, and the slit width governing the amount of light from the spectrometer decreased from 20 nm to 2 nm. Fit parameters could be found for wavelengths outside this range, but ZnO and ITO absorb below 400 nm and data collection did not extend far into the near-infrared. For these reasons, fit parameters were found only for the reflectances between 400 nm and 860 nm.

For smaller samples, the holder was modified with white vinyl tape to make the aperture a 12 mm square. Light hitting the vinyl tape of the modified sample holder caused an additional offset, now roughly 12 percentage points, as shown in Figure 36a.

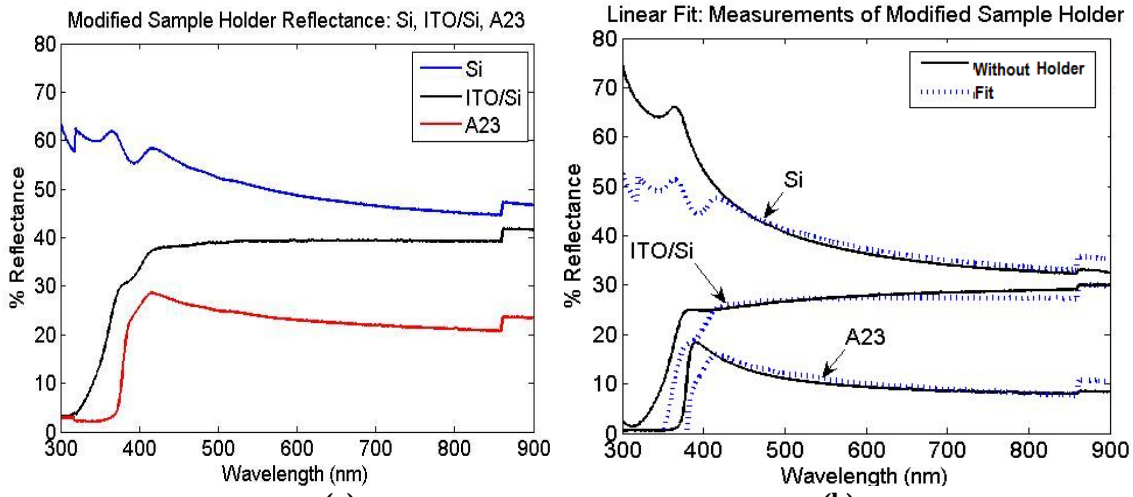

Figure 36. (a) Reflectances with modified sample holder. (b) Linear fit for the reflectances with the modified sample holder to those without the sample holder. β=1.063+/- 0.003 and γ = -14.4+/- 0.01.

The vinyl tape began to absorb near 450 nm leading to a sharp reduction in reflectances. Thus the linear fit was applied only between 450 nm and 860 nm. The fit parameters were found to be $\rho_{sample} = (\rho_{sphere}) \cdot .1.063 - 14.4$. The R^2 was 0.992.

A fit was attempted to incorporate the wavelength dependent reflectance of the sample holder with the white vinyl tape. The fit parameters β = 1.063 and γ=3.3+0.12$\cdot\rho_{tape}$ were used, where ρ_{tape} is the reflectance of the white vinyl tape, shown in Figure 37a. Accounting for the absorption at 450 nm by introducing the reflectivity of the white tape improved the entire fit.

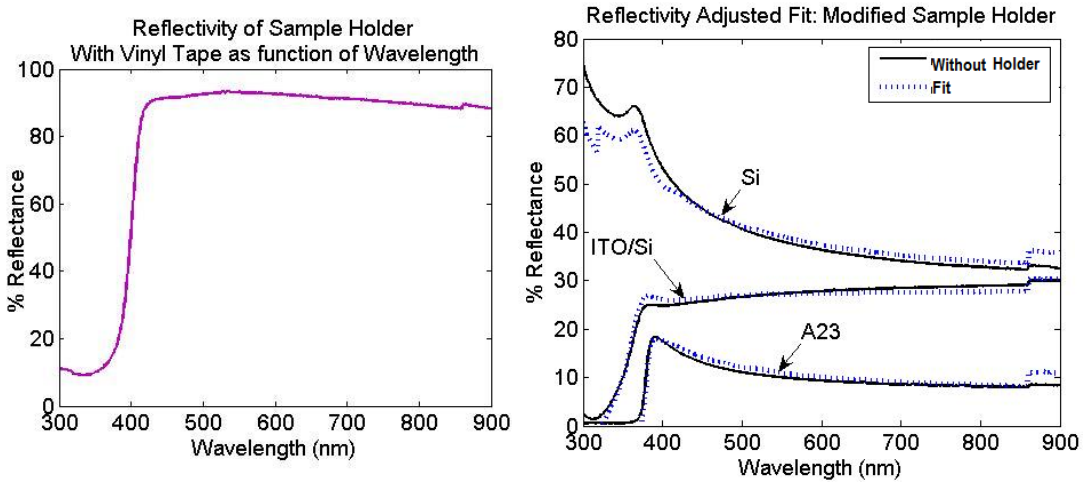

(a) **(b)**

Figure 37. (a) Reflectances for the tape used to modify the sample holder. (b) Fit for the reflectances with the modified sample holder accounting for the reflectances of the white tape. β=1.063 and γ = 3.3+0.12ρ_{tape} where ρ_{tape} is the reflectance of the tape.

The results shown in Figure 37 imply that fit parameters were more consistent with earlier results once the reflectance of the vinyl tape had been incorporated. As the reflectances were wavelength dependent, multiple regressions might have provided a better fit. Nonetheless, the simple linear fitting scheme appeared to work for wavelengths from 450 nm to 860 nm. As a result, the linear scheme was applied when comparing the relative reflectances of the samples measured using different holders. Both measured data and data fit using the parameters are reported below. In the results, reflectances calculated using the linear fit parameters associated with the sample holder were identified with "Fit 1". Reflectance calculated using the fit parameters incorporating the reflectivity for the modified sample holder were referred to as "Fit 2".

3.3.2 Total Reflectance

The reflectance spectra of vertical nanowires grown by ACG varied with the concentration of the bath, the number of zinc acetate seed layers, and the growth density of the wires.

The majority of ACG nanowire growth was performed with a 0.02 M bath concentration and grown for 4 hours. Figure 38 show the reflectance spectra for samples A14, A15, A16, A19 and A23, grown using these conditions. The figure shows measured spectra and the fits of the data to illustrate how the fit modified the amplitudes but only slightly modified the relative reflectance.

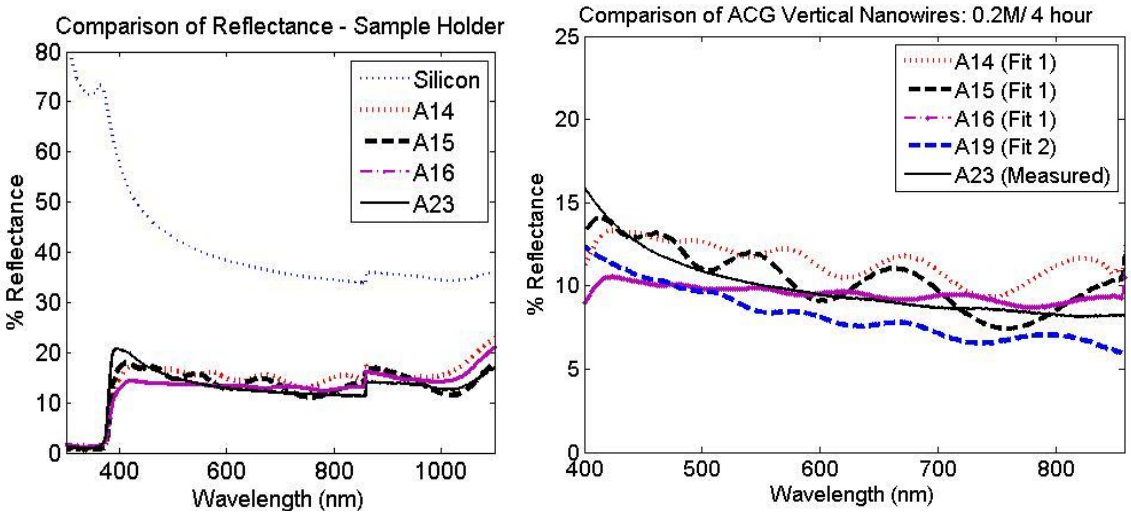

Figure 38. Reflectances for vertical nanowires grown by ACG in a 0.02 M bath for 4 hours. (a) Measurements with sample holder. (b) Fits to allow comparison of relative amplitudes.

The nanowires had average diameters of 55 nm to 100 nm. Sample A14 had 20 spray layers of zinc acetate, sample A20 had 10 spray layers and samples A16, A19, and A23 had 40 spray layers. As predicted, nanowires grown on a 40 spray, planar ZnO seed layer had lower average reflectance than nanowires grown on an inhomogeneous seed layer. This reduction in reflectance appeared to be unrelated to the nanowire diameters.

Thin film interference was probably the cause of the waviness in the reflectance spectra. Nanowire density, diameter, and length might all contribute to this effect. The larger number densities of nanowires had interference patterns with larger amplitudes. Figure 39 shows SEM images of sample A15, A14, and A16.

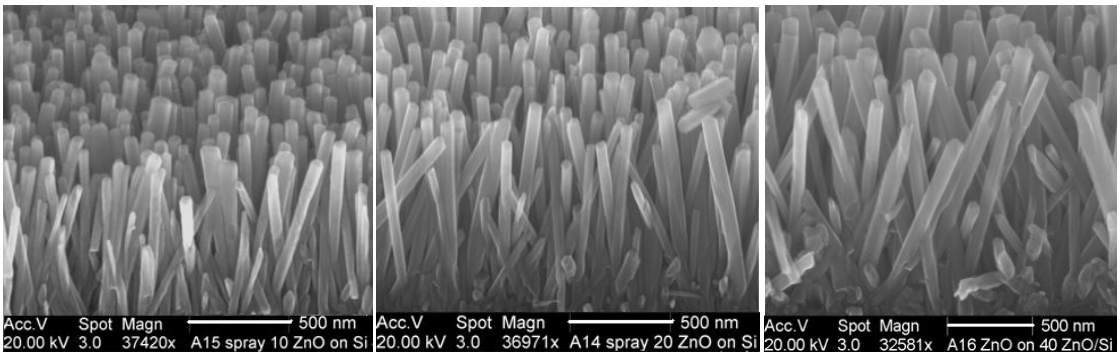

(a) A15 - 10 Spray **(b) A14 – 20 Spray** **(c) A16 – 40 Spray**

Figure 39. SEM images of vertical nanowires grown by ACG in 0.02 M baths.

Sample A15 had the smallest nanowire diameters and lengths, followed by samples A14 and A16. Nanowires with larger number densities appeared to have less vertical tilt than those with smaller number density. Vertical tilt may have caused additional scattering, eliminating the interference. Interference may also be associated with nanowire length.

The above comparison did not apply for the short, thin nanowires grown by ACG in a 0.01 M bath. Vertical nanowires grown in a 0.01 M bath for 5 hours had an average diameter of 30 nm and an average length of 400 nm. An example was shown in Figure 16c. The broadband reflectances for 0.02 M nanowires were significantly lower than the reflectances of nanowires grown in a 0.01 M bath. Figure 40 shows the reflectances for sample A23 grown in a 0.02 M bath and sample A20 grown in a 0.01 M bath.

A layer of TiO_2 was deposited on one sample between the planar ZnO layer and silicon. Since TiO_2 has a higher index of refraction than ZnO, it might improve the gradient index between the nanowires and the silicon. Sample A22 had a 50 nm layer of

TiO_2 between the planar ZnO layer and the silicon substrate, with nanowires grown in a 0.02 M bath for 4 hours on the planar ZnO. Figure 40 shows the reflectances of sample A22. Figure 40a shows measurements performed with the modified sample holder. Figure 40b shows the reflectances obtained using the fit parameters in order to compare the relative magnitudes.

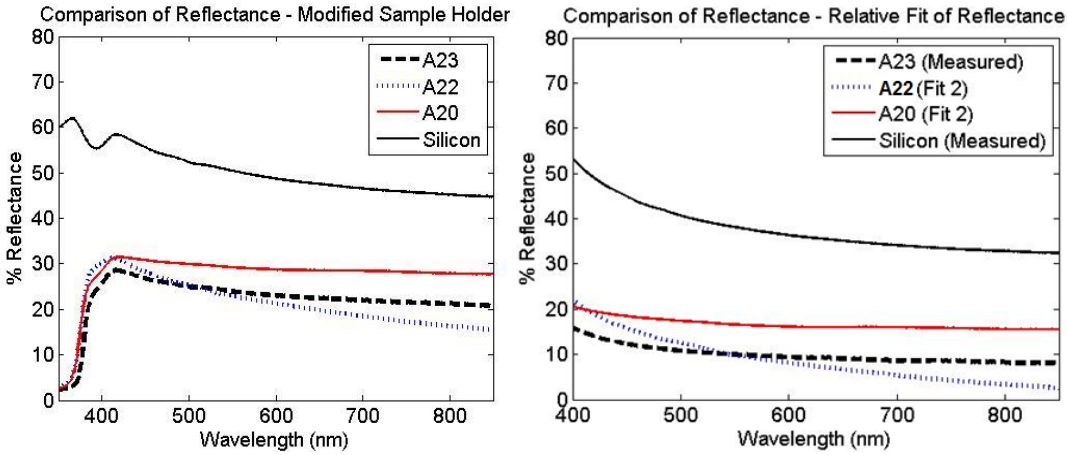

Figure 40. (a) Reflectances measured with modified sample holder for samples A23, A22, A20 and silicon. (b) Reflectances measured for sample A23 and for silicon compared with the fitted reflectances for samples A21 and A20.

The TiO_2 layer in sample A22 reduced the reflectance over only part of the spectrum, which may mean that layer thickness needs to be optimized.

Nanowires which were strong Lambertian scatterers, such as sample I1and I3 grown by electrodeposition, did not exhibit interference patterns. Sample I2, which did not have as much diffuse reflectivity, showed a waviness which may be associated with the thickness of the layer. Figure 41 shows the reflectances for randomly oriented samples grown by electrodeposited, silicon, and ITO/silicon.

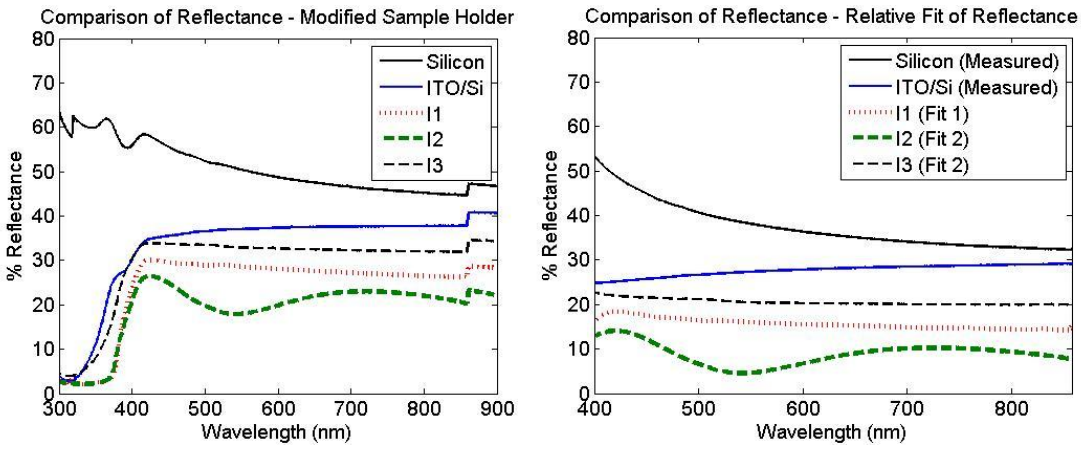

Figure 41. (a) Reflectance for electrodeposited samples mounted on the modified sample holder. (b) Fit of electrodeposited reflectances compared with ITO/Si and Si reflectances measured without a sample holder.

Figure 41a shows measurements taken with the modified sample holder and Figure 41b shows reflectances obtained using the fit parameters. Sample I3, with large ZnO flower like growth, had the highest reflectances of the three samples. Lambertian reflecting samples, samples I1 and I3, had uniform broadband reflectance. The reflectances for these samples were greater than the reflectances of sample I2. Sample I2, shown in Figure 21, had nanowires with an average diameter of 85 nm and length of 500 nm, less than half the average diameter and length of those for sample I1.

The reflectances for sample I2 were similar to those for the vertical nanowires samples. These samples had similar diameters and were also grown on a planar ZnO layer. Vertical nanowires and the randomly oriented nanowires of sample I2 had average reflectance of 8% to 15%. Nanowire orientation does not appear to affect the total reflectances, despite differences in scattering. Figure 42 shows the reflectances for a few vertical nanowires grown by ACG and for sample I2.

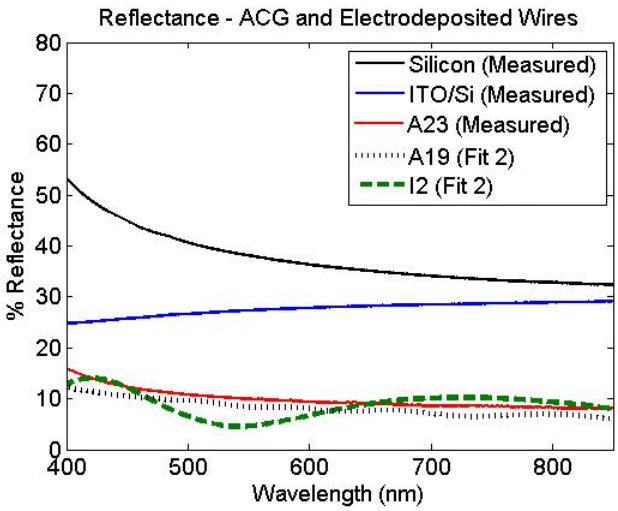

Figure 42. Reflectances for vertical ACG nanowire samples A19 and A23 and the electrodeposited randomly oriented sample I2.

Despite the measurement offsets introduced by the sample holders, qualitative and quantitative comparisons could be made for the broadband reflectances for the nanowire arrays. The best performing nanowire arrays reduced the broadband reflectance of silicon by a factor of five.

3.3.3 Angle Dependent Reflectance

Reflectances of ZnO nanowires on silicon were measured at angles of incidence incidence greater than 8^{o}. The measurements were performed with the Fluorolog III integrating sphere using a 12mm diameter center mount sample holder. The geometry of the sphere and the center mount allowed incident angles from 15° to 35°. Large entrance and exit ports and sample substitution error contributed to errors in the total reflectance calculations. Nonetheless qualitative comparisons of reflectances could be made for vertically and randomly arrayed nanowire samples.

The Fluorolog III was programmed for fluorescence measurements. Under normal control, the spectrometer sets the excitation wavelength and detects the scattered or fluoresced light over a range of wavelengths. For reflectance measurements, it was not possible to scan and detect at the same wavelengths. Consequently, the spectrometer was operated under real time control (RTC), by setting the wavelength and recording the instrument counts. The angle of incidence was changed by turning the knob which controlled the center mount, as shown in Figure 13a. For each wavelength and angle of incidence, data was collected three times and averaged. Appendix 2 presents a sample table for collected data.

Figure 43 shows the internal sphere geometry. To avoid reflecting light towards the emission port, the sample was turned counter-clockwise. The axis of rotation was near the edge of the sample. The sample holder encased the sample so that at incident angles greater than 35°, the incident light began to hit the sample holder. At 60° none of the incident beam illuminated the sample.

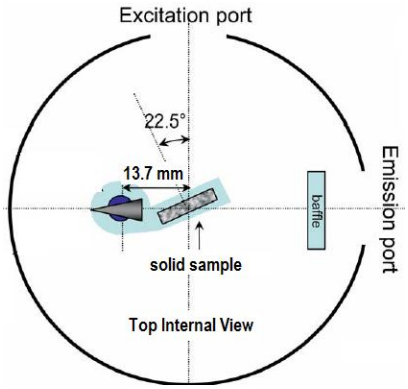

Figure 43. Internal view of Fluorolog III integrating sphere [43].

The sample holder and integrating sphere were covered with Spectralon©. The sample holder was shown in Figure 13b. The sample was placed in the holder so that it

faced toward the excitation port. Initially, reflectances for 8 samples were measured at 500 nm, including silicon and ITO/Si. At other wavelengths, only the vertical nanowire sample A19 and the randomly oriented sample I2, the samples of greatest interest, were measured. These samples had similar dimensions, yet different orientations. Measurements were performed at 300 nm, 400 nm, 500 nm, 650 nm, and 800 nm for incident angles of 15° to 60°. At 60° incidence, light hit the sphere wall and sample holder, thus providing the total reflectance of the sphere with the sample in place. To produce instrument counts in the range of 10^4 to 10^6, the slit width was varied from 1.47 nm to 3 nm.

The first reflectances were measured at 500 nm, as shown in Figure 44.

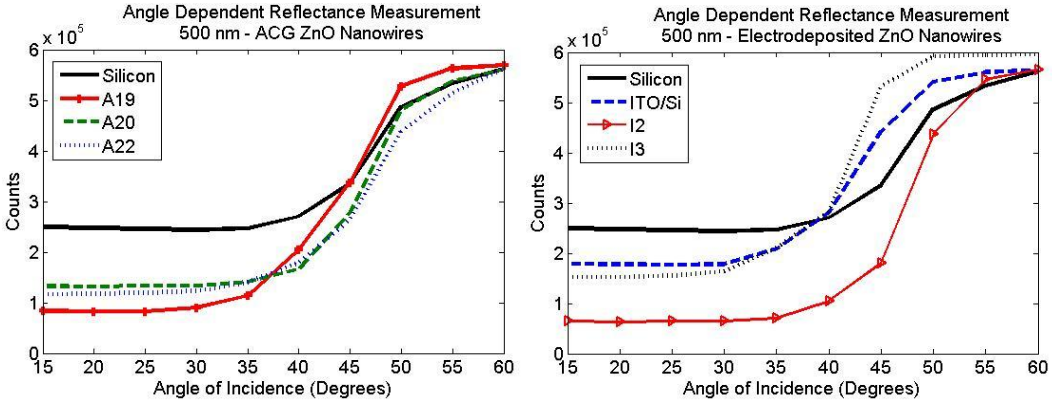

Figure 44. Angle dependent reflectances at 500 nm (a) vertical ACG nanowires and (b) randomly arrayed electrodeposited nanowires. Measurements performed with a slit width of 1.47 nm.

The light was unpolarized and therefore the reflectance of silicon should have remained constant for angles of incidence less than 65°, as was shown in Figure 29. The sharp increases in reflection for silicon between 35° and 40° indicated that light began to hit the sample holder. At angles less than 35° there were no significant variations in the reflectances for silicon, or for the nanowire samples. The reflectance obtained with the

Fluorolog III were roughly calculated by dividing the instrument counts recorded at 15° by those recorded at 60°, where the incident light did not hit the samples. Table 6 compares these reflectances to the measurements obtained with the Lambda 950 integrating sphere.

Table 6. Angle Dependent Reflectances at 500 nm

Sample	Angle	Silicon	ITO/Si	I2	I3	A19	A20	A22
Fluorolog % Reflectance	15°	44.5%	31.7%	11.4%	25.4%	14.8%	23.6%	20.7%
Lambda 950 % Reflectance	8°	40.8%	27.7%	6.6%*	21.4%*	9.7%*	17.5%*	12.6%*

* Calculated using Fit 2

There was a discrepancy between the reflectances of the samples provided by the two spheres. A correction factor may be needed for the Fluorolog III to account for sphere geometry and average wall reflectance. Since the Lambda 950 sphere could provide more reliable reflectance measurements due to its two-beam mode and size, the Fluorolog III was used to determine the relative reflectance change caused by changing the angle of incidence.

For the reflectances at other wavelengths, vertical nanowire sample A19 and randomly oriented nanowire sample I2 were compared. For all wavelengths, there were negligible changes in the reflectance with changing angles of incidence for angles smaller than 35°. Figure 45 shows their relative reflectances. For measurements at 300 nm and 800 nm the slit width was 3 nm. All other wavelengths were measured with a slit width set at 1.42 nm.

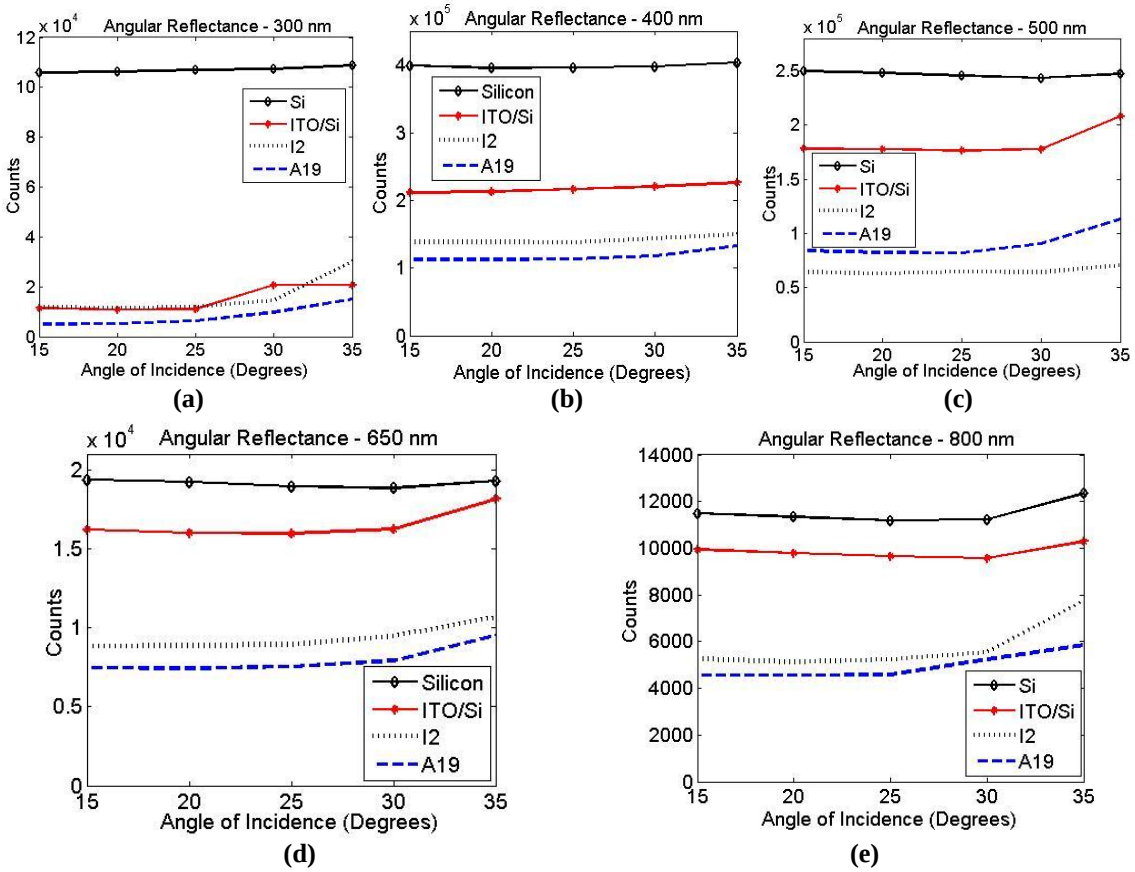

Figure 45. Angle dependent reflectances at wavelengths of (a) 300 nm. (b) 400 nm. (c) 500 nm. (d) 650 nm. and (e) 800 nm.

At 300 nm, very low instrument counts were observed for A19, I2, and ITO/Si. The small reflectances were associated with the absorption by these samples. Although the absolute amplitudes of the reflectances were not determined, the relative reflectances of samples I2 and A19 were consistent with those measured by the Lambda 950 integrating sphere, as was shown in Figure 40. At 400 nm, 650 nm, and 800 nm, vertical nanowire sample A19 had a lower reflectance than sample I2. At 500 nm, on the other hand, sample I2 had a lower reflectance. Ideally, measurements would have been performed at angles of incidence greater than 35°. The increase in the reflectance of silicon for incident angles greater than 65° suggests that measurements at larger angles of

incident were necessary. Owing to equipment limitations, however, it was not possible to perform total reflectance measurements at angles of incidence greater than 35°.

3.5 Theoretical Comparison

Various methods are used to model the reflectances of the nanowire arrays. The simplest uses an effective media approximation (EMA) for the nanowire layer. Effective media approximations are based on a random unit cell distribution of two materials [47]. The transfer of light, however, is dependent on the size, shape, and spatial distribution of cells. The critical minimum thickness of the layer for which the EMA becomes valid is 50 times the nanowire diameter [27]. A film thickness of 4.5 μm is much greater than the average 900 nm length of nanowire samples, which had typical diameters of 85 nm. Nonetheless, the EMA has been employed by several researchers. Chen et al. [18] successfully modeled the interference of highly uniform GaN nanowire arrays based on the volume-fill of the nanowires. Diedenhofen et al. [21] used EMA to model GaP nanorods. Another method to model the nanowires is Rigorous Coupled Wave Analysis (RCWA). It solves Maxwell's equations for a 2-D grating structure [48]. To account for the nanowire morphology and scattering, however, solving Maxwell's equations in three-dimensions would be the most accurate approach.

Even though the EMA method fails to account for the effects of nanowire size and geometry on light scattering, it remains the simplest method. Consequently, it was used in this study to model the reflectances of the ZnO nanowire arrays. SEM images were used

to determine the height variation of the nanowires. Figure 46 shows the height variation for sample A12, vertical nanowires grown by ACG.

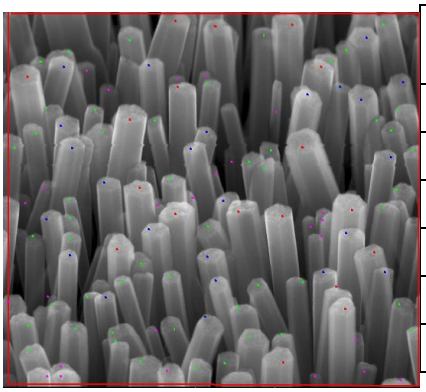

Level	Max. Height	Fractional area	Fractional Volume	Index of Refraction
1	960	.1070	. 11	1.09
2	860	.2129	.21	1.18
3	760	.3514	.35	1.33
4	660	.3892	.39	1.36
5*	460	.5892	.58	1.56
6	60	1	1	2

* Inferred from side view of wires

Figure 46. Nanowire height variations for Sample A12. The fractional area and volume apply to each area and were used to determine the index of refraction. Fractional area and volume determined from the average diameter and number of nanowires present in that layer.

The average diameter, height of the layer, and number of nanowires in the layer, were used to find the fractional volume. The fractional volume of ZnO, f_{ZnO}, was used in the EMA to find the effective index of refraction, n_{eff}, for the layer:

$$f_{ZnO}\frac{n_{Zno}^2 - n_{eff}^2}{n_{Zno}^2 + 2n_{eff}^2} + (1 - f_{ZnO})\frac{n_{air}^2 - n_{eff}^2}{n_{air}^2 + 2n_{eff}^2} = 0$$

For simplicity, the wavelength dependence of the index of refraction for ZnO was not taken into account. The index of refraction of ZnO varies only slightly for visible light, from n = 1.9 to n = 2.1. An index of refraction of n = 2 was assumed in the EMA calculations. Figure 47 shows the calculated reflectance for a TE wave for the 6-layer and 10-layer gradient-index films.

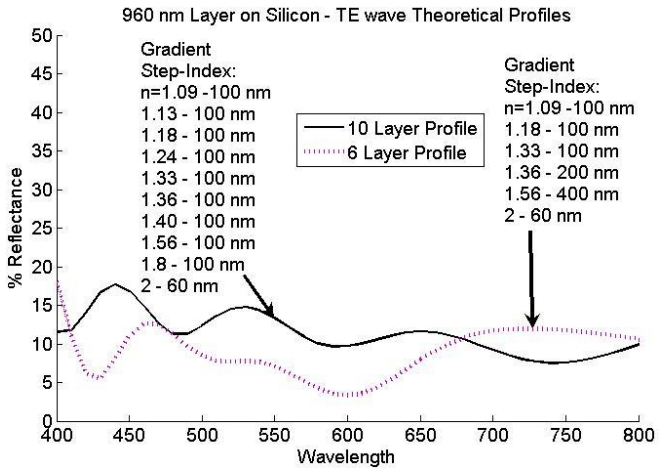

Figure 47. Theoretical reflectances for 10- and 6- gradient layers of a 960 nm thick film calculated by the transfer-matrix using MATLAB.

The 6-layer gradient layer was dissimilar to reflectances experimentally found for vertical nanowires. The conclusion was that 6-layers were too coarse to model the nanowire morphology. By stratifying the 6 layers into 10 layers, with a total thickness of 960 nm, a reflectance profile similar to that of vertical nanowire sample A15 was obtained. Figure 48 compares the reflectances calculated for the 10 gradient layer film to those measured for sample A15.

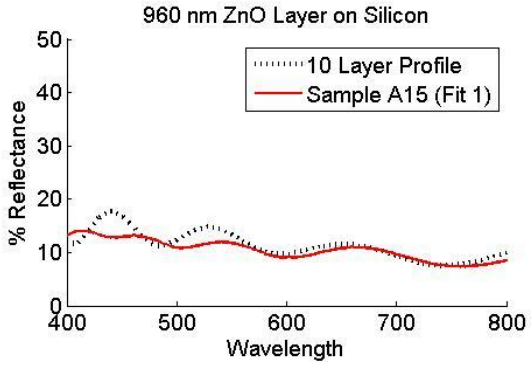

Figure 48. Reflectances measured for the vertical nanowire sample A15 and calculated for a 10-gradient layer film.

The modeled reflectances were similar to the experimental values. Errors determining the height profiles and the sensitivity of the reflectances to small changes in

the height profile suggested that the modeling process will require further investigation. The modeling requires better measures of the height profile, such as those obtained using an Atomic Force Microscope (AFM). Nonetheless, the EMA was useful when estimating the reflectance changes caused by adding additional layers to a sample profile, as for example in the case of the TiO_2 layer added to vertical nanowire sample A22.

4. Summary of Results and Conclusions

ZnO nanowire arrays significantly reduced the broadband reflectance of silicon. Nanowires that were grown by ACG and electrodeposition had distinct morphologies. The morphology of the nanowires influenced their reflectivity. Vertical nanowires grown by ACG had relatively small diffuse reflectivity and relatively large specular reflectivities. Randomly arrayed nanowires grown by electrodeposition exhibited greater diffuse reflectivity and less specular reflectivities than the vertical nanowire samples.

Total reflectance measurements compared the reflectances of ZnO nanowires on a silicon substrate to the reflectances of a bare silicon substrate. Large, diffusely scattering nanowires and ZnO crystals did not perform as well as smaller nanowires at reducing the reflectance for silicon. Despite differences in diffuse and specular reflection, alignment of nanowires did not appear to determine reflectance. Vertical nanowires grown in a 0.02 M concentration bath and randomly arrayed electrodeposited nanowires had similar reflectances when grown on a planar ZnO layer. These ZnO arrays had average diameters between 60 nm and 100 nm, and average lengths between 500 nm and 1100 nm. They created a 30 percentage point reduction in the total reflectance of silicon, a five-fold decrease. Shorter, thinner nanowires reduced the broadband reflectance of silicon by half, or 20 percentage points. Large, thick crystal growth reduced the broadband reflectance of silicon by an average of 15 percentage points.

The reflectances for the ZnO nanowire arrays were constant at angles of incidence less than 35°. Measurements of the total reflectance of the nanowires at higher angles of incidence are still needed.

The relative power density transmittances of the ZnO nanowires were compared to those of an idealized single layer AR coating of ZnO, optimized for solar irradiance at 520 nm. Figure 49 shows the Global air mass 1.5 spectral irradiance and the reflectances for a single layer ZnO AR coating and vertical ZnO nanowires. The spectral irradiance was obtained from the American Society for Testing and Materials (ASTM). The spectrum includes direct and diffuse irradiance for a tilted surface in the northern hemisphere, and is a standard for the photovoltaic industry [49]. The total power density from 250 nm to 4000 nm is 895 W/m^2.

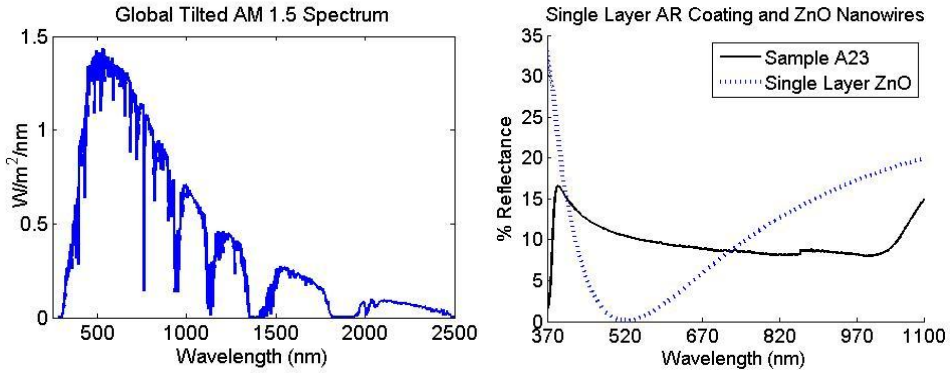

(a) **(b)**

Figure 49. (a) Spectral irradiance in the Northern Hemisphere, tilted spectrum with a total irradiance of 895 W/m^2 (b) Reflectances for vertical ZnO nanowire sample A23 on silicon, and for a theoretical single layer ZnO AR coating, *n* = 2, on silicon.

Table 7 presents the spectral irradiance that would be transmitted by three different ZnO nanowire samples and a single ZnO layer optimized for 520 nm. The total irradiance in Table 7 is provided for two different ranges of wavelengths. Both the single layer ARC and the ZnO nanowires reflect much less energy than a bare silicon substrate. For the lower range of wavelengths, the single layer AR coating perfomed better than the ZnO nanowires. For a wavelength range extended to 1100 nm, the ZnO nanowire array performed as well as the single layer AR coating.

Table 7. Transmittance of Solar Irradiance (895 W/m^2)		
Material	**Wavelengths 400 nm – 900 nm Total Irr.= 564 W/m^2**	**Wavelengths 400 nm -1100 nm Total Irr.= 677 W/m^2**
Silicon	353 W/m^2	437 W/m^2
ZnO SLARC	529 W/m^2	620 W/m^2
ZnO A23 Sample	509 W/m^2	610 W/m^2
ZnO I2 Sample	516 W/m^2	621 W/m^2
ZnO A19 Sample	518 W/m^2	620 W/m^2

However, low energy photons with wavelengths above 1000 nm will not be strongly absorbed by silicon. Shown in Figure 50 is the absorption of bare silicon. A multi-crystalline solar cell will have an overall higher absorption due to doping, back surface reflectors, and surface passivation, but a similar decrease in the absorption for photons above 1000 nm due to the bandgap of silicon at 1.1 eV.

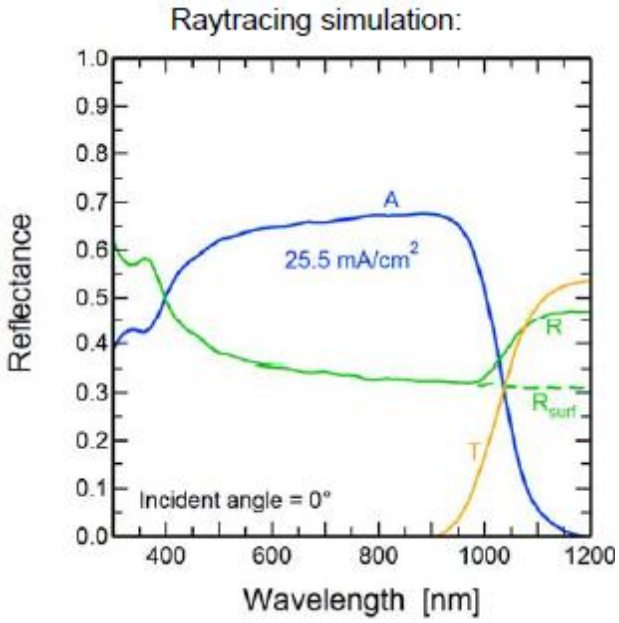

Figure 50. Raytracing simulation of an Air→Silicon→Air layer. The absorption, A, decreases at longer wavelengths since the band-gap of silicon is 1.1eV [50].

The comparison illustrates the need to reduce reflection by the ZnO nanowire arrays at wavelengths near the maximum for solar irradiance, from 500 nm to 600 nm, to be optimized for a silicon substrate.

The transmittance of the AR coatings should also be compared for a range of incident angles. There was little change in the reflectances for either the theoretical single layer ZnO AR coating or the measured ZnO nanowires for angles of incidence below 35°. The transmittance of a single layer AR coating begins to degrade for large angles of incident light. At 65°, power density transmitted falls to 596 W/m^2 for the 400 nm to 1100 nm wavelength range. The transmittance of ZnO vertical and randomly arrayed nanowires is unknown for high angles of incidence. Measurements are still needed of reflectances by nanowire arrays at large angles of incidence.

Results from this research agree with those found by Chen and Sun [24] and Lee et al. [25], shown in Figure 51.

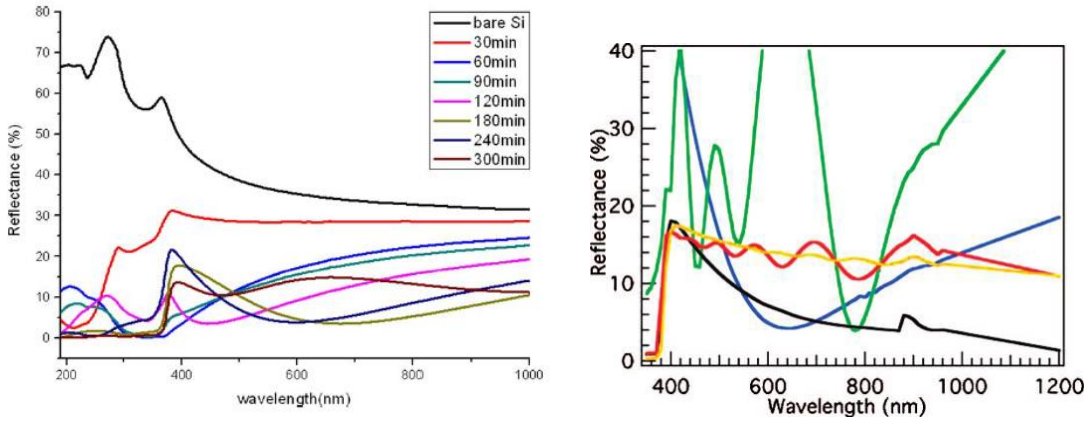

(a) **(b)**

Figure 51. (a) Reflectances of nanowires grown by Chen and Sun [24]. Concentration of bath between 0.01M to 0.04M. Nanowire growth times as listed. (b) Reflectances of nanowires grown by Lee et al. [25]. Flat top nanowires (red), tapered nanowires (gold), and highly tapered nanowires (black). Blue indicates a single layer AR coating on a solar cell.

Reflectances for the ZnO nanowires grown by ACG and by electrodeposition, which were shown in Figure 42, compared favorably with those obtained by a 240 min ZnO nanorod sample grown by Chen and Sun, and with the flat top nanowires grown by Lee et al. The reflectances of the nanowires in this study, however, were not as small as the tapered nanowire reflectances shown in Figure 51b.

A reduction in the reflectance by ZnO nanowires at visible wavelengths would be the best way to increase the transmittance of light into the substrate. Random height variation of the nanowires may not be sufficient to create an optimal gradient-index AR coating. Lee et al. created the tapered nanowires by introducing a hazardous chemical agent, diaminopropane (DAP), into the zinc nitrate and methenamine chemical bath. A less toxic, low temperature method might be found to create similar tapering. For instance, galvanostatic electrodeposition of ZnO nanowires from a zinc nitrate solution, in the presence of potassium hydroxide and sodium hydroxide, also lead to tapered nanowire tips. The drawback of electrodeposition is that it requires a conductive substrate. The aqueous chemical growth is thus the preferred large scale method.

Further knowledge of the scattering properties of nanowires is necessary to determine whether nanowires will improve the efficiency of solar cells over the use of traditional AR coatings. Creation of a simple silicon solar device on which to test the ZnO nanowires would be the best way to make comparisons. Another approach would be to improve the modeling techniques for the nanowire arrays. Broadband total reflectances for ZnO nanowires have been successfully measured. Characterization of the nanowires

at large angles of incidence is still needed to determine their viability as directional AR coatings.

REFERENCES

[1] Archer M.D. Clean Electricity from Photovoltaics, Series on Photoconversion of Solar Energy – Vol 1. Archer M, Hill R, editor, London: Imperial College Press; 2001. 844 p.

[2] Green MA. "Self-consistent optical parameters of intrinsic silicon at 300 K including temperature coefficients". Solar Energy Materials & Solar Cells. July 2008; 92: 1305–1310.

[3] Yablonovich E, Cody G. "Intensity Enhancement in Textured Optical Sheets for Solar Cells." IEEE Tran. on electron devices. Feb. 1982; 29: 300-304.

[4] Thorp D, Wenham S R. "Ray-tracing of arbitrary surface textures for light-trapping in thin silicon solar cells." Solar Energy Materials and Solar Cells. 1997; 48: 295-301.

[5] Willeke G, Nussbaumer H, Bender H and Bucher E."A simple and effective light trapping technique for polycrystalline silicon solar cells". Solar Energy Materials and Solar Cells. 1992; 26 : 345-356.

[6] Bennet, CA. Principles of Physical Optics. Hoboken, N.J.: Wiley, 2008. 492 p.

[7] Born M, Born E, et al. Principles of Optics: electromagnetic theory of propagation, interference and diffraction of light. Oxford; New York : Pergamon Press, 1980. 809 p.

[8] Pedrotti FL, Pedrotti LS. Introduction to Optics. Englewood Cliffs, N.J.: Prentice-Hall,1987. 551 p.

[9] Markvart, T. and Castañer, L. Practical Handbook of Photovoltaics: Fundamentals and Applications. Oxford: Elsevier Advanced Technology, 2003. 984 p.

[10] Moore DT. "Gradient-index optics: a review". Applied Optics. 1 April 1990; 19: 1035-1038.

[11] Lord Rayleigh, "On reflection of vibrations at the confines of the two media between which the transition is gradual". Proceedings of the London Mathematical Society. 12 February 1980; 11: 51-60.

[12] Bergner BC, Germer TA, Suleski TJ. "Effective medium approximations for modeling optical reflectance from gratings with rough edges" Journal of the Optical Society of America, A. May 2010; 27: 1083-1010.

[13] Southwell WH. "Gradient-index antireflection coatings". Optics Letters. November 1983; 8: 584-586.

[14] Poitras D and Dobrowolski JA. “Toward perfect antireflection coatings. 2. Theory” Applied Optics. 20 February 2004; 43: 1286-1295.

[15] Chen M, Chang H, Chang ASP, Lin SY, and Xi JQ. “Design of optical path for wide-angle gradient-index antireflection coatings”. Applied Optics. 10 September 2007; 43: 6533-6538.

[16] Southwell WH and Sankur H. “Broadband gradient-index antireflection coating for ZnSe”. Applied Optics.15 August 1984 ; 23: 2770-2773.

[17] Kuo ML, Poxson D, Kim YS et al. “Realization of a near-perfect antireflection coating for silicon solar energy utilization”. Optics Letters. 1 November 2008; 33: 2527-2529.

[18] Chen HY et al. “Gallium nitride nanorod arrays as low refractive-index transparent media in the entire visible spectral region”. Optics Express. 26 May 2008; 16: 8106-8116.

[19] Huang YF, et al. “Improved broadband and quasiomnidirectional anti-reflection properties with biomimetic silicon nanostructures”. Nature Nanotechnology. 2 December 2007; 2: 770-774.

[20] Kanamori Y, Sasaki M and Hane K. “Broadband antireflection gratings fabricated upon silicon substrates”. Optics Letters. 15 October 1999; 24: 1422-1425.

[21] Didenhofen SL, et al. “Broad-band and Omnidirectional Antireflection Coatings Based on Semiconductor Nanorods.” Advanced Materials. 2009; 21: 973–978.

[22] Yu Z, Raman A and Fan S. “Fundamental limit of light trapping in grating structures”. Optics Express. 13 September 2010 ; Vol. 18: A366-A380.

[23] Musken OL, Rivas JG, Algra RE, Bakkers E, and Lagendijk A. “Design of Light Scattering in Nanowire” NanoLetters. July 2008; 8: 2638-2642.

[24] Chen JY and Sun KW. “Growth of vertically aligned ZnO nanorod arrays as antireflection layer on silicon solar cells”. Solar Energy Materials and Solar Cells. 22 January 2010; 94: 930–934.

[25] Lee YJ, Ruby DS, Peters DW, McKenzie BB and Hsu JWP. “ZnO Nanostructures as Efficient Antireflection Layers in Solar Cells.” NanoLetters. 2008; 8: 1501-1505.

[26] Moharam MG, Pommet DA, and Grann EB. “Stable implementation of the rigorous coupled-wave.” Journal of the Optical Society of America, A. 1995; 12: 1077-1086.

[27] Braun MM and Pilon L. “Effective optical properties of non-absorbing nanoporous thin films.” Thin Solid Films. 2006; 496: 505-514.

[28] Jagadish C and Coleman VA. Zinc oxide bulk, thin films and nanostructures: processing, properties and applications. Editors Jagadish C and Pearton S. Hong Kong: Elsevier; 2006. 589 p.

[29] Nadarajah, Athavan. Electroluminescence from annealed and un-annealed electrodeposited ZnO nanowires. Masters of Science Thesis. Portland State University. 2006; 90 p.

[30] Kittel C. Introduction to Solid State Physics, Eigth edition. Hoboken, NJ: Wiley and Sons; 2005. 680p.

[31] Vayssieres L, Keis K, Lindquist SE, and Hagfeldt A. “Purpose-Built Anisotropic Metal Oxide Material: 3D Highly Oriented Microrod Array of ZnO.” Journal of Physical Chemistry, B. 2001; 105: 3350-3352.

[32] Willander M, et al. “Zinc oxide nanorod based photonic devices: recent progress in growth, light emitting diodes and lasers” Nanotechnology. 28 July 2009; 332001: 332040.

[33] Xu S, Lao C, Weintraub B and Wang ZL. “Density-controlled growth of aligned ZnO nanowire arrays by seedless chemical approach on smooth surfaces.” Journal of Materials Research. August 2008; 23: 2072-2077.

[34] Vayssieres, L. “Growth of arrayed nanorods and nanowires from aqueous solutions.” Advanced Materials. 4 March 2003; 15: 464-466.

[35] Vernardou D, Kenanakis G, Couris S, Koeoumas E, Kymakis E and Katsarakis N. “pH effect on the morphology of ZnO nanostructures grown with aqueous chemical growth.” Thin Solid Films. 1 April 2007; 515: 8764–8767.

[36] Li Q, Kumar V, Li Y, Zhang H, Marks T and Chang R. “Fabrication of ZnO Nanorods and Nanotubes in Aqueous Solutions.” Chemical Materials. 1 February 2005; 17: 1001-1006.

[37] Baruah S and Dutta J. “pH-dependent growth of zincoxide nanorods”. Journal of Crystal Growth. 4 February 2009; 311:2549–2554.

[38] Greene LE, Law M, Tan DH, Montano M, Goldberger J, Somorjai G, and Yang P. “General Route to Vertical ZnO Nanowire Arrays Using Textured ZnO Seeds.” NanoLetters. 18 June 2005; 5: 1231-1236.

[39] Krunb M and Mellikov E. “Zinc oxide thin films by the spray pyrolysis method.” Thin Solid Films. 1 December 1995; 270: 33-36.

[40] Peulon S and Lincot D. “Mechanistic Study of Cathodic Elecfrodeposition of Zinc Oxide and Zinc Hydroxychioride Films from Oxygenated Aqueous Zinc Chloride Solutions” Journal of the Electrochemical Society. March 1998; 145: 864:874.

[41] LabSphere. “A Guide to Integrating Sphere Theory and Applications.” Technical Application. Available from: http://www.labsphere.com/technical/technical-guides.aspx 18 April 2011; 19p.

[42] Perkin Elmer application notes. “Applications and Use of Integrating Spheres With the LAMBDA 650 and 850 UV/Vis and LAMBDA 950 UV/Vis/NIR Spectrophotometers”. Available from: http://www.perkinelmer.com. 2 March 2010.

[43] Horiba Jobin Yvon. “Integrating Sphere, F-3018 Operation Manual, Part number 81089 version 1.2.” Integrating Sphere. 3 Jul 2008; 44 p.

[44] Storm S, Springsteen A, Ricker T. “The Use of Center Mount Sample Holders in Reflectance Spectroscopy”. LabSphere Application Note 2. January 1998; 8p.

[45] Green, MA and Keevers MJ. “Optical properties of intrinsic silicon at 300 K” Progress in Photovoltaics: Research and Applications. 1995; 3: 189–192.

[46] Filmetrics: Refractive Index Database. Available from: http://www.filmetrics.com/refractive-index-database. 21 April 2010.

[47] Niklasson GA and Granqvist CG. “Optical properties and solar selectivity of coevaporated Co-AI20 3 composite films” Journal of Applied Physics. 1 May 1984; 55: 3382-3410.

[48] Moharam MG, Pommet DA, Grann EB, and Gaylor Tk. “Stable implementation of the rigorous coupled-wave analysis for surface-relief gratings: enhanced transmittance matrix approach.” Journal of the Optical Society of America. May 1995; 12: 1077-1076.

[49] Reference Solar Spectral Irradiance: ASTM G-173. National Renewable Energy Laboratory. Available from: http://rredc.nrel.gov/solar/spectra/am1.5/ASTMG173/ASTMG173.html. 21 May 2011

[50] Altermatt, Pietro. Special Topics in Solar Cells, Portland State University. 25 July 2010. Day 3, Photogeneration, pg 5.

6. Appendices

6.1 Appendix 1

ZnO nanowires grown by ACG and Electrodeposition.

ZnO Sample Preparation by Aqueous Chemical Growth (ACG) on Silicon							
No.	**Date**	**ID**	**Solution**	**Pre-Growth**	**Temp. (^oC)**	**Time**	**NOTES:**
1	5/26/2010	A1	.05M Zinc Nitrate/.05M methenamine	20 sprays Zinc acetate (every 30 sec) at 300deg / Anneal 380deg 20min	85-90	1hr	Spray left funny blue residue. Too much heat?
2	5/26/2010	A2	.05M Zinc Nitrate/.05M methenamine	20 sprays Zinc acetate (every 30 sec) at 300deg / Anneal 380deg 20min	85-90	3hr	Evaporation. After 1hr - only 400ml (instead of 500ml) was there. After 3 hr, 200ml
3	5/26/2010	A3	.05M Zinc Nitrate/.05M methenamine	No	85-90	1hr	
4	5/26/2010	A4	.05M Zinc Nitrate/.05M methenamine	No	85-90	3hr	
5	6/2/2010	A5	.02M Zinc Nitrate/.02 methenamine	20 sprays Zinc acetate (every 30 sec) at 300deg / Anneal 380deg 20min	85-90	3hr	Initial Ph 5.77 ;
6	6/2/2010	A6	.02M Zinc Nitrate/.02 methenamine	No	85-90	3hr	80C Ph: 4.83
7	6/23/2010	A7	.1M Zinc Nitrate/ .15 meth.	no	90	1hr	10x the concentration. Added 5ml NH3 solution for pH
8	6/24/2010	A8	.02M Zinc Nitrate/.02 methenamine	10 sprays Zinc acetate (every 30 sec) at 280deg / Anneal 380deg 20min	85-90	5hr-2sol.	40ml , covered with thermometer. No stir. Ph dip test ~6 ; Change to new solution after 3hours. Very Uniform looking growth
9	6/30/2010	A9	.02M Zinc Nitrate/.02 methenamine	10 sprays Zinc acetate (every 30 sec) at 280deg / Anneal 380deg 20min	85-95 (Avg. 90)	4hr	40ml, covered, face down, slowly add solution (3ml or less /time), to maintain volume and T

ZnO Sample Preparation by Aqueous Chemical Growth (ACG) on Silicon							
No.	**Date**	**ID**	**Solution**	**Pre-Growth**	**Temp. (°C)**	**Time**	**NOTES:**
10	7/7/2010	A10	.02M Zinc Nitrate/.02 methenamine	10 sprays Zinc acetate (every 30 sec) at 280deg / Anneal 380deg 20min	85-95 (Avg. 90) - more variation	4hr	40ml, covered, no stir, slowly add more solution. New hot plate- more variability. Solution older, more white platelets.
11	7/8/2010	A11	.02M Zinc Nitrate/.02 methenamine	5 sprays Zinc acetate (every 30 sec) at 280deg / Anneal 380deg 20min	85-95 (Avg. 90)	4hr	40ml, covered, no stir, good angle, didn't monitor temp. Slowly add solution. New Solution
12	7/13/2010	A12	.02M Zinc Nitrate/.02 methenamine	40 sprays Zinc acetate (every 30 sec) at 280deg / Anneal 380deg 20min	-95	4hr	40ml, good angle, boiled for about 10min after half hour. Started A13 AT THIS POINT. Slowly add solution. Boil again…
13	7/13/2010	A13	.02M Zinc Nitrate/.02 methenamine	40 sprays Zinc acetate (every 30 sec) at 280deg / Anneal 380deg 20min	88	4hr	40ml, covered, small piece, had to prop up. Did not monitor temp CONSISTENTLY LOWER THAN A12!!!
14	7/20/2010	A14	.02M Zinc Nitrate/.02 methenamine	20 sprays Zinc acetate (every 30 sec) at 280deg / Anneal 380deg20min	85-95 (Avg. 90)	4hr	40ml, covered, no stir, good angle,Good temperature control, usually below 90C avg 87C
15	7/20/2010	A15	.02M Zinc Nitrate/.02 methenamine	10 sprays Zinc acetate (every 30 sec) at 280deg / Anneal 380deg 20min	85-95 (Avg. 90)	4hr	Good temperature control, usually below 90C avg 87C (not monitored)
16	7/28/2010	A16	.02M Zinc Nitrate/.02 methenamine	40sprays Zinc acetate (every 30 sec) at 280deg / Anneal 380deg 20min	85-95 (Avg. 90)	4hr	

ZnO Sample Preparation by Aqueous Chemical Growth (ACG) on Silicon							
No.	**Date**	**ID**	**Solution**	**Pre-Growth**	**Temp. (^{o}C)**	**Time**	**NOTES:**
17	4/2/2011	A19	.02M Zinc Nitrate/.02 methenamine	40sprays Zinc acetate (every 30 sec) at 280deg / Anneal 380deg 20min	85-90	4hr	40ml, covered, no stir. Avg 87C. Large sample size, overall good coverage.
18	4/14/2011	A20	.01M Zinc Nitrate/.02 methenamine	40sprays Zinc acetate (every 30 sec) at 280deg / Anneal 380deg 20min	90	5hr	Good temperature control 90C. Appears like little or no wire growth
19	4/15/2011	A21	.02M Zinc Nitrate/.02 methenamine	4 turns TiO2 10% vol in ISP at 2500RPM,/30sec, anneal 5min at 250C and 380deg 1 hr. 40sprays Zinc acetate (every 30 sec) at 280deg / Anneal 380deg 20min	90	4hr	Thick, non uniform TiO2 layer - Good wire growth
20	4/20/2011	A22	.02M Zinc Nitrate/.02 methenamine	1 turn TiO2 10% vol in ISP at 2500RPM,/30sec, anneal 5min at 100Cand 380deg 1 hr. 40sprays Zinc acetate (every 30 sec) at 280deg / Anneal 380deg 20min	88-92	4hr	Thin TiO2 layer.
21	5/11/2011	A23	.02M Zinc Nitrate/.02 methenamine	40sprays Zinc acetate (every 30 sec) at 280deg / Anneal 380deg 20min	88-92	3.75hr	Growth on large silicon substrate. Good nanowire coverage, not entirely uniform across large substrate area.

Electrodeposited ZnO Nanowires on ITO/ Glass						
No.	**Date**	**ID**	**SAMPLE**	**Preparation**	**Anneal**	**Remarks**
1	11/18/2009	G1	ZnO/ITO WIRES	Electrodeposition ZnCl/KCl/AlCl3; 3600s; -1.00V; 80degC	2hr @ 380C	Stubby Wires
2	11/25/2009	NA	ZnO/ITO Planar	Spray 45 Layers	2hr @ 380C	Didn't Work - Not hot enough at 180C
3	12/16/2009	G2	ZnO/ITO WIRES	Electrodeposition ZnCl/KCl/AlCl3; 3600s; -1.05V; 80degC	2hr @ 380C	Good wires- SEM image files
4	1/4/2010	G3	ZnO/ITO WIRES	Electrodeposition ZnCl/KCl/AlCl3; 3600s; -1.10V; 80degC	2hr @ 380C	Contamination; Platelets formed.
5	1/8/2010	NA	ZnO/ITO Planar	Spray 43 Layers of Zinc Acetate at 280deg	1hr @ 380C	Uniform Deposition; transparent but unknown thickness
6	2/4/2010 and 2/5/2010	G4	ZnO/ITO Planar with ZnOSpray	Electrodeposition ZnCl/KCl/AlCl3; 3600s; -1.05V; 80degC; Spray 30 layers at 280degC	2hr @ 380C	SEM images - thick wires with some scattered ZnO on top
7	2/10/10 and 2/11/10	G5a	ZnO/ITO Planar with PVK spin coat	Electrodeposition ZnCl/KCl/AlCl3; 3600s; -1.05V; 80degC; Spin coat with PVK dilute with Chloroform (10g/l)	UV light 2*5min	2 drop coats and spins
8	2/10/10 and 2/11/10	G5b	ZnO/ITO Planar with TiO2 drop	Electrodeposition ZnCl/KCl/AlCl3; 3600s; -1.05V; 80degC; Drop coat TiO2 nanoparticles at 50degC; blow off excess	2hr @ 380C	Drop coat 1 time

Electrodeposited ZnO Nanowires on ITO/Silicon						
No.	**Date**	**ID**	**SAMPLE**	**Pre-growth**	**Growth**	**Notes**
1	7/22/2010	I1	ZnO/ITO/Si	None	Electrodeposition ZnCl/KCl/AlCl3; 3600s; -1.05V; 80degC;	Problem with electrode at first. Current roughly 9e-3.
2	4/6/2011	I2	ZnO/ZnO/ITO/Si	40 sprays zinc acetate	Electrodeposition ZnCl/KCl/AlCl3; 3600s; -1.05V; 80degC;	Current roughly 5e-3 A
3	4/13/2011	I3	ZnO/ITO/Si	none	Electrodeposition ZnCl/KCl/AlCl3; 3600s; -1.05V; 80degC;	Current roughly 4e-3A

6.2 APPENDIX 2

Example of sngle depedent reflectance measurements measured using Fluorolog III.

Silicon - 500nm					
Angle	**1**	**2**	**3**	**Avg.**	**STDEV**
15	249691	250236	249997	249974.67	273.18553
20	247982	248085	247828	247965	129.34064
25	245550	246131	245507	245729.33	348.51734
30	243075	244349	243661	243695	637.68017
35	247631	247037	246838	247168.67	412.5704
40	270762	269821	270510	270364.33	487.1184
45	335227	335548	335962	335579	368.47931
50	487962	486893	487463	487439.33	534.89282
55	534133	532962	533308	533467.67	601.60646
60	560867	562692	562887	562148.67	1114.2299

6.3. **APPENDIX 3**

Example of Tranfer Matrix Method (TMM) code written for MATLAB to find the total reflectances of layers.

```
%% matrix_R_tot_substratechange.m
clear M del k p q j t totmat lambda R Rq totq Q  index_no gos goi
anglemat beta clear layer index  d r t qtrans qr trans lambda
hold off

layer=[100;100;100;100;100;100;100;100;100;40;60] %Thickness of layers
index=[1.09;1.13;1.18;1.24;1.33;1.36;1.40;1.56;1.7;2;2.7;4.2]; %Index
of refraction of layers.

s1=si(:,1:2);%Si is a 81x2 matrix with wavelength dependent indices of
                  refraction.
index_no=1; %Index of incident media

angle=0; %Angle of incidence

sz=size(index,1);

count=1;

for lambda=250:10:1100; %Calculate for each wavelength
    clear r p1  m22 m21 m12 totmat M j beta p q k beta p q trans
index_no=1;

gos=find(s1(:,1)==lambda);
index(sz,1)=s1(gos,2); %Make the index of refraction of silicon the
last layer.

anglerad=angle*2*pi/360; %Change to radians

for g=1:size(index,1);
    anglemat(g,1)=asin((index_no*sin(anglerad))/index(g,1));
%Propagation of angle.
end

for j=1:size(index,1)-1; %Index is the actual refractive indices of
each layer
                      %layer gives the thickness of each layer
%This gives the characteristic matrix of each layer.

      k=2*pi/(lambda);
      beta(j,1)=k*layer(j,1)*index(j,1)*cos(anglemat(j,1));
      p(j,1)=(index(j,1))*cos(anglemat(j,1)); %TE wave
      q(j,1)=(1/index(j,1))*cos(anglemat(j,1)); %TM wave

%TE wave
```

```
  M(1,1,j)=cos(beta(j,1));%m11, matrix j
  M(1,2,j)=-i*(1/p(j,1))*sin(beta(j,1)); %m12, matrix j
  M(2,1,j)=-i*(p(j,1))*sin(beta(j,1)); %m21, matrix j
  M(2,2,j)= cos(beta(j,1)); %m22, matrix j


%TM wave
  Q(1,1,j)=cos(beta(j,1));%m11, matrix j
  Q(1,2,j)=-i*(1/q(j,1))*sin(beta(j,1)); %m12, matrix j
  Q(2,1,j)=-i*(q(j,1))*sin(beta(j,1)); %m21, matrix j
  Q(2,2,j)= cos(beta(j,1)); %m22, matrix j

  clear k
end

%Now there are matrices stored in M(X,j) which can be used to multiply
%together and Q(X,j)

clear totmat tot1

totmat=eye(2,2); %TE wave

tot1=eye(2,2); %TM wave

for g=1:size(index,1)-1;
totmat=totmat*M(:,:,g);
totq=tot1*Q(:,:,g);

end

clear Q M

%The reflection is given by the following....transfer first to last
%layer using the elements of totmat.

m11=totmat(1,1); %TE
m12=totmat(1,2);
m21=totmat(2,1);
m22=totmat(2,2);

x11=totq(1,1); %TM
x12=totq(1,2);
x21=totq(2,1);
x22=totq(2,2);

p1=(index_no(1,1))*cos(anglemat(1,1)); %this gives the incident element
ps=(index(size(index,1),1))*cos(anglemat(size(index,1),1)); % this
gives the last element

q1=(1/(index_no(1,1)))*cos(anglemat(1,1));
qs=(1/index(size(index,1),1))*cos(anglemat(size(index,1),1));
```

```
r=(((m11+(m12*ps))*p1)-
(m21+(m22*ps)))/((m11+(m12*ps))*p1+(m21+(m22*ps)));
trans=(2*p1)/(((m11+(m12*ps))*p1)+(m21+(m22*ps)));


qr=(((x11+(x12*qs))*q1)-
(x21+(x22*qs)))/((x11+(x12*qs))*q1+(x21+(x22*qs)));
qtrans=(2*q1)/(((x11+(x12*qs))*q1)+(x21+(x22*qs)));

R(count,1)=abs(r)^2;
T(count,1)=(ps/p1)*(abs(trans))^2;

Rq(count,1)=abs(qr)^2;
Tq(count,1)=(qs/q1)*(abs(qtrans))^2;


clear p1 ps qs q1 r trans qr qtrans
count=count+1;
end

lambda=250:10:1100;
plot(lambda',R*100,'g');
hold on
plot(lambda',Rq*100,'r');
hold on
plot(lambda',100*(R+Rq)/2,'k');


%%%%%%%%%%%%
```